A METHOD FOR DETERMINING PAPER PROCESSING PARAMETERS USING TERAHERTZ SPECTROSCOPY

by

Ian Bushfield
BSc. (Engineering Physics), University of Alberta, 2009

THESIS SUBMITTED IN PARTIAL FULFILLMENT OF
THE REQUIREMENTS FOR THE DEGREE OF

MASTER OF SCIENCE

in the
Department of Physics
Faculty of Science

SIMON FRASER UNIVERSITY

Fall 2011

APPROVAL

Name:	**Ian Bushfield**
Degree:	**Master of Science (Physics)**
Title of Thesis:	***A Method for Determining Paper Processing Parameters Using Terahertz Spectroscopy***

Examining Committee:

Chair: David Broun, Associate Professor

J. Steven Dodge
Senior Supervisor
Associate Professor

Erol Girt
Supervisor
Associate Professor

Karen Kavanagh
Supervisor
Professor

Frank Haran
Internal Examiner
Honeywell

Date Defended/Approved: 8 December 2011

Partial Copyright Licence

The author, whose copyright is declared on the title page of this work, has granted to Simon Fraser University the right to lend this thesis, project or extended essay to users of the Simon Fraser University Library, and to make partial or single copies only for such users or in response to a request from the library of any other university, or other educational institution, on its own behalf or for one of its users.

The author has further granted permission to Simon Fraser University to keep or make a digital copy for use in its circulating collection (currently available to the public at the “Institutional Repository” link of the SFU Library website (www.lib.sfu.ca) at http://summit/sfu.ca and, without changing the content, to translate the thesis/project or extended essays, if technically possible, to any medium or format for the purpose of preservation of the digital work.

The author has further agreed that permission for multiple copying of this work for scholarly purposes may be granted by either the author or the Dean of Graduate Studies.

It is understood that copying or publication of this work for financial gain shall not be allowed without the author’s written permission.

Permission for public performance, or limited permission for private scholarly use, of any multimedia materials forming part of this work, may have been granted by the author. This information may be found on the separately catalogued multimedia material and in the signed Partial Copyright Licence.

While licensing SFU to permit the above uses, the author retains copyright in the thesis, project or extended essays, including the right to change the work for subsequent purposes, including editing and publishing the work in whole or in part, and licensing other parties, as the author may desire.

The original Partial Copyright Licence attesting to these terms, and signed by this author, may be found in the original bound copy of this work, retained in the Simon Fraser University Archive.

Simon Fraser University Library
Burnaby, British Columbia, Canada

revised Fall 2011

ABSTRACT

To ensure consistency, paper manufacturing requires knowledge of the thickness, areal density, and moisture content of a paper sheet as it is produced. In this thesis, I show that it is possible to use terahertz time-domain spectroscopy to estimate these three parameters. I relate the electromagnetic response of paper to its composition based on an effective medium model that includes an additional term to account for Rayleigh scattering. I show results from Monte Carlo simulations that establish statistical limits on the parameter estimates for this model under realistic conditions, and I assess the performance of the model using experimental results on pulp samples. Finally, I discuss current limitations to the precision of this measurement technique, and suggest methods for improving it.

To those who made this work possible:
my parents and my loving wife

We have a habit in writing articles published in scientific journals to make the work as finished as possible, to cover up all the tracks, to not worry about the blind alleys or describe how you had the wrong idea first, and so on. So there isn't any place to publish, in a dignified manner, what you actually did in order to get to do the work"

-Richard Feynman, Nobel Lecture, 1966

ACKNOWLEDGEMENTS

Without the help, support, and encouragement that I have received over the course of this degree, this thesis may have never been completed. In particular, I want to thank…

- **Jeff McGuirk** for his understanding when I changed my mind and pursued a different path;
- **Steve Dodge** for giving me the chance to complete this degree and the support through this entire process;
- **Amir Farhani** for helping me learn to use this terahertz spectrometer;
- **Payam Mousavi** for his assistance learning the two-parameter model;
- **Frank Haran**, **David Jez**, **Stéphane Savard,** and the rest of the staff at Honeywell for supporting me and this project, and keeping me busy through the summer of 2011;
- **Laleh Mohtashemi** for help building the new terahertz mounts and working on the spectrometer;
- **Graham Lea**, **Derek Sahota**, and **Anthony Steigvilas** for keeping the office interesting;
- my many other friends in the department and at SFU for their support;
- **Sonia Milbradt** for her unwavering love and support;
- Sonia’s parents for a comfortable place to live in Vancouver; and
- my family for their continued support.

TABLE OF CONTENTS

LIST OF FIGURES

LIST OF TABLES

LIST OF SYMBOLS

c	Speed of light – 299 792 458 m/s
ϵ	Relative permittivity
ϵ_0	Permittivity of free space – 8.8542 x 10^{-12} F/m
n	Index of refraction
α	Optical absorption coefficient [m^{-1}]
$\mathbf{E}$	Terahertz electric field
$\mathbf{T}$	Complex transmission amplitude
ν	Volume fraction
f	Frequency [THz]
ω	Angular frequency = $2\pi f$
t	Time [ps]
d	Thickness (or caliper) [μm]
M	Mass moisture content [%]
BW	Basis weight [g/m^2 or gsm]
τ	Scattering particle size [μm]
σ	Standard deviation
SNR	Signal-to-noise ratio
Subscripts	(a) air, (w) water, (dry) dry content, (f) fibre, (r) reference, (s) sample

1: MOTIVATION

1.1 Terahertz spectroscopy and its applications

The terahertz region of the electromagnetic spectrum corresponds to wavelengths in the sub-millimetre range and frequencies of 100 GHz to a few THz. Terahertz frequencies fall between the upper limits of electronics technology and the lower limits of conventional optical systems, and for this reason has been called the terahertz gap [1]. Until the mid-1990s, material parameters in a region of the electromagnetic spectrum remained largely unexplored.

Recent work has demonstrated a wide range of scientific and technological applications of terahertz radiation [2]. Terahertz time-domain spectroscopy relies on radiation generated in single-cycle pulses with widths of about a picosecond and bandwidths of one to several terahertz. These wavelengths are ideal for probing the conductivity of semiconductors and metals in thin films [3]. Many plastics and fabrics absorb very little in the terahertz regime, making terahertz radiation useful for non-contact imaging such as in airport full-body scanners [1]. Terahertz also has practical applications in industrial quality control applications, where wiring inside an integrated circuit can be inspected non-destructively.

1.2 Sensing technology for paper processing parameters

Paper is fabricated from a mixture of wood and recycled pulp, ash, and water. Terahertz radiation is strongly absorbed by water and only weakly absorbed by most organic molecules, making it an ideal candidate for sensitive, non-contact measurements of paper. Accurate and precise sensors are necessary for paper manufacturing because control over composition and thickness is essential for fabricating a product of consistent quality.

Important control parameters in paper processing include caliper, basis weight, and moisture content. Caliper refers to the thickness of a sheet, measured in microns. Basis weight is typically specified on commercially available paper and is a measure of the mass per unit area, measured in grams-per-square-metre (gsm). Basis weight can be measured both with (wet) or without (dry) the mass of water included. In this thesis I refer only to the wet basis weight. Finally, moisture content is a percentage measure of the water mass content of a sheet.

Measurements in a working paper mill are taken from a stage that scans back and forth over moving paper sheets. These in-line measurements rely on several different technologies to measure each of the parameters. For example, Honeywell currently offers products to measure caliper with magnetic inductance, moisture content with infrared or microwave radiation, and basis weight with absorption of nuclear beta radiation [4] [5] [6].

1.3 Terahertz spectroscopy for paper processing parameter sensing

One possible advantage of using terahertz to measure paper parameters is that three measurement technologies could be replaced with a single sensor. Terahertz techniques are well suited to this problem as the components of paper have well-understood behaviour in the terahertz frequency regime. This thesis will show how the electromagnetic properties of paper can be related to parameters of interest to the paper processing industry.

Mousavi et. al. demonstrated that by modelling paper as a mixture of water and dry content, they could simultaneously measure the thickness and moisture content of paper with terahertz spectroscopy [7]. I will show in this thesis that by adding a third component to their model, I can estimate caliper, moisture content, and basis weight simultaneously. Honeywell's current targets are to measure basis weight to an accuracy of ± 0.25 gsm with a precision of ± 0.1 gsm; moisture content to an accuracy of ± 0.25% with a precision of ± 0.1%; and caliper to an accuracy of ± 1 μm with a precision of ± 0.1 μm.

2: TERAHERTZ APPARATUS

This chapter will outline the basic elements of our terahertz spectrometer, before discussing our method for extracting physical parameters with it. The terahertz spectroscopy system that I used for the measurements in this thesis is located in the Dodge lab at Simon Fraser University and was originally developed by Carl-Philippe Kübler [8]. Full details of the spectrometer can be found in Kübler's thesis.

2.1 Spectrometer

Terahertz pulses for our experiments are generated and detected in the time-domain using an ultrafast laser and photo-conducting antennas. We measure the electric field of a terahertz pulse in the time-domain. The Fourier transform of a pulse transmitted through a paper sample can be related to the sample's physical characteristics.

Figure 1 shows the basic layout of the spectrometer. The spectrometer relies on an ultrafast laser system to generate and detect the terahertz pulses. A near-infrared pulse from the ultrafast laser is split evenly by the beam splitter. One portion of this pulse is focussed onto the emitter antenna, while the other is focussed onto the detector antenna. The detection pulse passes through a physical delay stage, which allows the path length of this arm to be changed with respect to the emitter arm. The terahertz beam is collected, collimated, and focussed by four off-axis parabolic mirrors. Parabolic mirrors, unlike Teflon lenses, do not absorb higher frequencies.

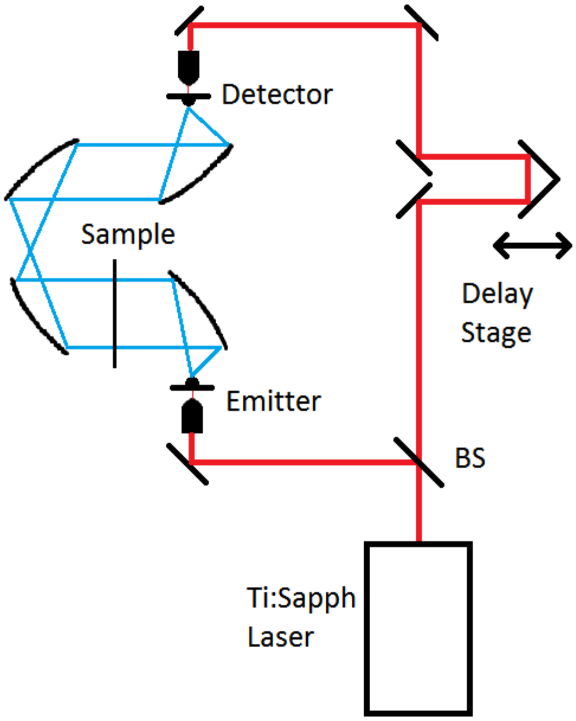

Figure 1 – Layout of our terahertz time-domain spectrometer. A titanium-sapphire (Ti:Sapph) ultrafast laser source provides excitation pulses for the terahertz emitter and detectors via a beam splitter (BS). An off-axis parabolic mirror collimates the terahertz beam (blue) from the emitter before it passes through the sample. More parabolic mirrors guide the terahertz beam to the detector. An adjustable delay stage changes the path length of the detector arm, allowing time-domain detection of the terahertz pulse.

2.1.1 Ultrafast laser system

The backbone of spectrometer is a KM Labs titanium sapphire (Ti:Sapph) oscillator. This laser produces a beam with a centre wavelength of 780 nm, an average power of 500 mW, 80 fs duration pulses, and a repetition rate of 80 MHz. Half of the total laser power is used for the terahertz spectrometer, while the rest is used for other experiments in the lab. The ultrafast beam is divided roughly equally between the emitter and detector arms.

2.1.2 Terahertz generation

Terahertz pulses in our lab are generated with a photoconductive antenna structure illustrated schematically in Figure 2. The primary element in the structure is an aluminum thin-film Hertzian dipole, 50 μm long, running vertically in the figure. A 10 μm gap at the centre of the antenna is connected by a photoconducting silicon underlayer that prevents current from flowing when photocarriers are not present. The entire dipole is connected to the outside world through a parallel wire transmission line, 1 cm long, shown running horizontally in the figure between contact pads. The antenna was fabricated on a silicon-on-sapphire (SOS) wafer at SFU using an etching process described in Kübler's thesis [8]. To improve the signal-to-noise ratio at high frequencies, the wafers were then subjected to ion implantation, which reduces the carrier trapping time in the silicon underlayer [9], [10]. The implantation was delivered in two doses, the first at 100 KeV and the second at 200 KeV with areal densities of 10^{15} cm^{-2}, at CORE systems[1].

A modulated bias field of 20 V_{rms} is applied across the gap to provide the excitation energy for the terahertz pulse. The modulation allows for phase-sensitive detection, described in the next section. An ultrafast laser pulse excites carriers in the semiconductor substrate to the conduction band, effectively short-circuiting the gap. The bias field rapidly accelerates charges across the gap, which generate an electromagnetic field proportional to the time derivative of the induced surface current $E \propto \partial j / \partial t$ [11], illustrated by Figure 3. The initial current pulse can exhibit reflections from electrical boundaries, so the transmission line structure is designed to match the impedance of the antenna. Reflections from the contact pads are then delayed in time and can be windowed out in the time domain.

---

[1] http://www.coresystems.com

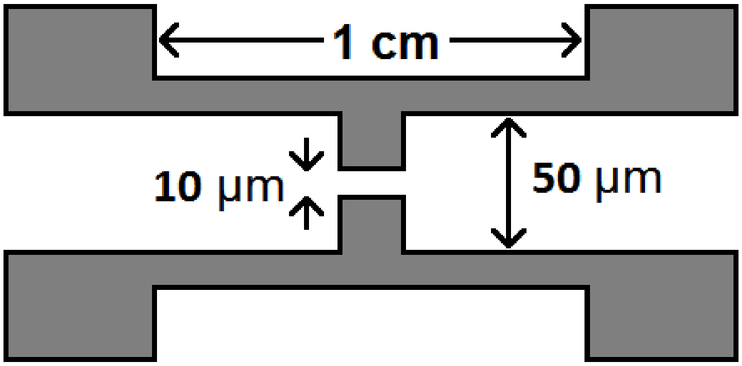

Figure 2 – Schematic of the photoconductive antenna. The antenna consists of a 50 μm metal dipole with a 10 μm gap fabricated on a silicon-on-sapphire wafer.

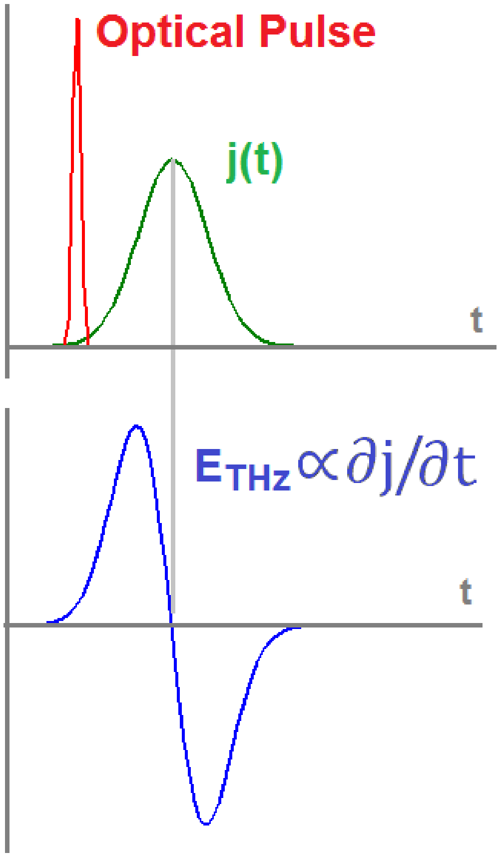

Figure 3 – Illustration of terahertz generation. An external bias voltage drives a photocurrent *j(t)* consisting of carries excited by an optical pulse (top). The radiated terahertz field E_{THz} is proportional to the time derivative of the photocurrent (bottom).

The emitter radiates preferentially into the sapphire substrate. The terahertz pulse from the emitter is collected by a high-resistivity silicon hyper-hemispheric lens, which better couples the radiation from the substrate to free space. The lens has a 5 mm radius of curvature and a total thickness of 5.962 mm. This geometry reduces the numerical aperture of the emitter, allowing the terahertz beam to be almost entirely collected by an off-axis parabolic mirror [8]. Silicon is used for the lens because it exhibits low absorption and little dispersion between 0.2 and 2.0 THz [12].

2.1.3 Terahertz detection

Crudely, our detection scheme can be understood as running our generation technique in reverse: whereas an external bias drives a photocurrent in the emitter to radiate a terahertz pulse, in the detector the terahertz pulse provides a bias that induces a measurable current via optically-excited photocarriers. To accomplish this, we direct the terahertz pulse on a second radiation-damaged SOS photoconductive antenna. Simultaneously, the second portion of the near-infrared pulse, split at the beam splitter, is focussed onto the detector antenna gap. This shorter pulse is timed to coincide with the arrival of a portion of the terahertz pulse at the detector, so that photocarriers in the detector are accelerated in proportion to the instantaneous terahertz electric field. In this way, the near-infrared pulse essentially gates the terahertz waveform with a 600 fs window width that is set by the carrier lifetime. The photocurrent is the convolution of the terahertz pulse and the photocarrier density and is typically measured in picoamperes. The current is converted by a low-noise transimpedance amplifier to a more easily measurable voltage. The timing of the near-infrared pulse is controlled by a linear delay stage in the beam's path. As this path length shifts, the near-infrared pulse shifts with respect to the terahertz electric field in time, allowing for time-sensitive detection, as illustrated by Figure 4.

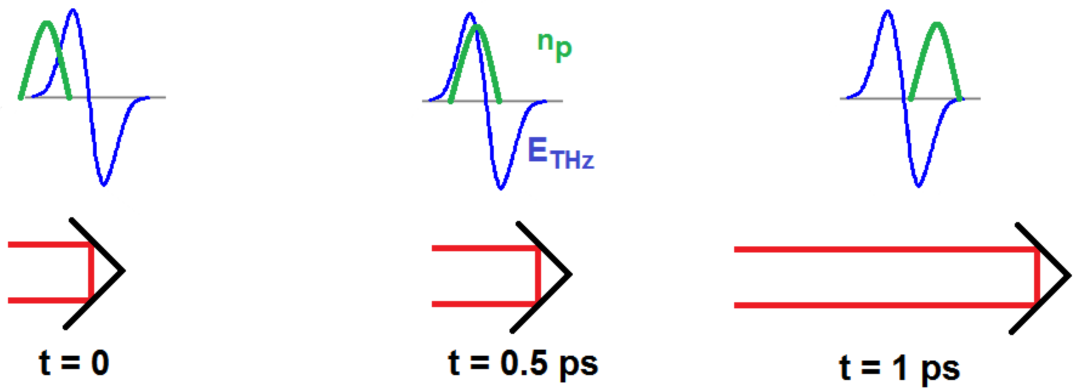

Figure 4 – Illustration of coherent gated detection. The measured current is a convolution of the terahertz electric field (blue) and the photocarrier density n_p (green). As the delay stage is moved (bottom), the detection beam changes the delay between the two pulses, thereby sampling the entire terahertz pulse in time.

Each near-infrared laser pulse generates a corresponding terahertz pulse, so our terahertz repetition rate is also 80 MHz. By biasing the emitter with a 20 V_{rms} sinusoidal wave at a much lower frequency of 1 kHz, we create an envelope of terahertz pulses, illustrated in Figure 5. These slowly-changing pulses can then be measured using lock-in detection [13]. Our lab employs an EG&G Instruments 7265 DSP Lock-In Detector.

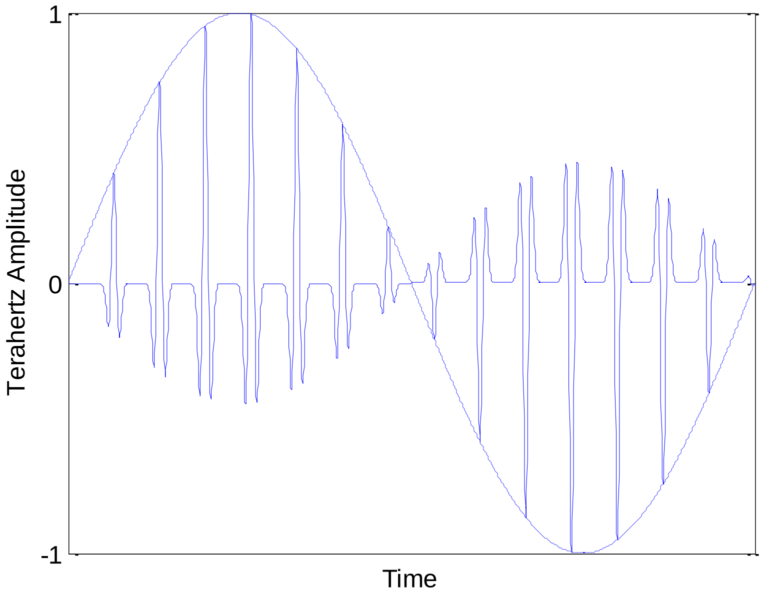

Figure 5 – Illustration of terahertz modulation (repetition rates are not to scale). Dotted line shows modulated emitter bias voltage.

2.1.4 System characteristics

To characterize our system after alignment, I recorded fifty terahertz pulses while the spectrometer was enclosed in an acrylic box purged with nitrogen. The nitrogen purge removes most of the water vapour from the terahertz beam path, thereby reducing absorption lines. Figure 6 shows the 50 overlapped terahertz pulses in the time- and frequency-domain. The width of the pulse at half the maximum amplitude is 1 ps. The bandwidth, defined by the point when the spectral amplitude decays to the noise floor, is 1 THz. The noise floor is the mean amplitude of the high-frequency noise.

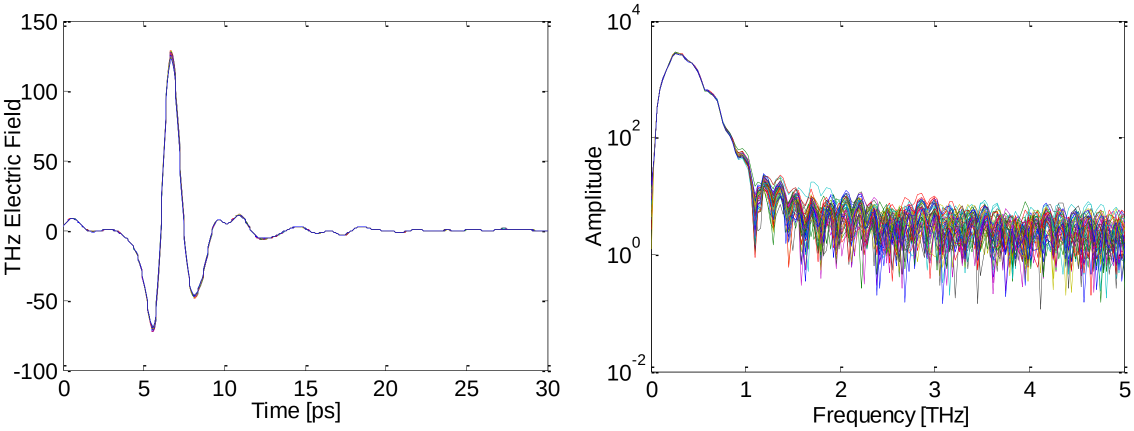

Figure 6 –Typical terahertz pulses in time (left) and frequency (right) domain. These fifty pulses were taken under a nitrogen purge.

Low-frequency time-domain noise can produce a time-base shift of the terahertz pulse that varies from one time trace to the next, as expressed by

$$\mathbf{E}_{n+1}(\omega) = e^{i\eta\omega}\mathbf{E}_n(\omega)\,. \tag{1}$$

A least-squares fit to equation (1) for the set of fifty pulses shown in Figure 6 gives an estimate of 2.5 fs from the standard deviation in η.

For this thesis, I worked with Laleh Mohtashemi to design new mirror mounts, described in Appendix A, that decreases this time-based drift and eases alignment. I also performed a simulation and analysis of the optical layout, described in Appendix B.

2.2 Extracting physical parameters from a sample

To determine physical properties of a sample such as the absorption and dispersion, we need a framework to relate the electric field of a terahertz pulse that propagates through free space with one that traverses a sample.

At normal incidence, the transmission coefficient for electromagnetic radiation travelling from a medium of index n_1 into a medium of index n_2 is

$$t_{12} = \frac{2n_1}{n_1 + n_2}, \tag{2}$$

while the corresponding reflection coefficient is

$$r_{12} = \frac{n_1 - n_2}{n_1 + n_2}. \tag{3}$$

In a medium with refractive index n and absorption coefficient α, both potentially frequency-dependent, an electromagnetic wave at a location d in the medium is

$$\mathbf{E} = e^{-\alpha d/2} e^{i\omega n d/c} \mathbf{E}_0, \tag{4}$$

where $\mathbf{E_0}$ is the initial electric field amplitude and ω is the frequency of the wave.

Accounting for internal reflections, the transmitted electric field $\mathbf{E_s}$ will be

$$\mathbf{E}_s = t_{12}\left(e^{-\alpha d/2} e^{i\omega n d/c}\left(1 + r_{21}^2 e^{-\alpha d} e^{2i\omega n d/c} + r_{21}^4 e^{-2\alpha d} e^{4i\omega n d/c} + \ldots\right)\right) t_{21} \mathbf{E}_i, \tag{5}$$

which can be rewritten with equations (2) and (3) as

$$\mathbf{E_s} = \frac{t_{12} t_{21} e^{-\alpha d/2} e^{i\omega n d/c}}{1 - r_{21}^2 e^{-\alpha d} e^{2i\omega n d/c}} \mathbf{E_i} \tag{6}$$

using the series expansion for $(1-x)^{-1}$. A reference pulse travels an equivalent distance d through air

$$\mathbf{E_r} = e^{i\omega d/c} \mathbf{E_i}. \tag{7}$$

Dividing equation (6) by (7) yields an expression for the index, absorption, and thickness in terms of the measured waveforms,

$$\mathbf{T}=\frac{\mathbf{E_s}}{\mathbf{E_r}}=\frac{\dfrac{4n}{(n+1)^2}e^{-\alpha d/2}e^{i\omega(n-1)d/c}}{1-\dfrac{(n-1)^2}{(n+1)^2}e^{-\alpha d}e^{2i\omega nd/c}}. \qquad (8)$$

In the next chapter, I will show how this equation, together with an effective medium theory for paper can be used to determine paper process parameters.

3: TERAHERTZ PROPERTIES OF PAPER

This chapter will develop a model that will relate paper process parameters – caliper, moisture content, and basis weight – to optical parameters that can be measured with terahertz time-domain spectroscopy. I then use Monte Carlo simulations to obtain insight into the fundamental limitations on the sensitivity of this technique.

3.1 Effective medium theories

When electromagnetic radiation is incident on a heterogeneous dielectric like paper, the external field will not be the same as the local field inside the medium. The incident electric field will polarize individual molecules in the mixture, which then induce their own field in the surrounding material. This field will further polarize the constituent molecules, which then induce an additional field, and so forth. A simple equation for the exact response cannot be written down, but several effective medium theories have been proposed to provide a simple analytic description of the macroscopic response.

The response of a mixture can be determined by averaging the electric field over volumes larger than the inhomogeneities. In this limit, the mixture is effectively homogenous and isotropic with respect to an incident electric field **E** and the relative effective permittivity ϵ can be characterized such that

$$\mathbf{D} = \epsilon\epsilon_0\mathbf{E}, \tag{9}$$

where $\boldsymbol{D}$ is the electric displacement field and ϵ_0 is the permittivity of free space.[2] This effective permittivity can be calculated for different limiting cases.

---

[2] In this thesis, all permittivities ϵ refer to dimensionless relative permittivities, except ϵ_0, the permittivity of free space, which is 8.8542 x 10^{-12} F/m.

In previous work on a two-parameter model of paper, Mousavi et. al. relied on the effective medium theory of Bruggeman to relate the constituent permittivities to that of mixture ϵ by solving [7]

$$\nu_w \frac{\epsilon_\mathrm{w} - \epsilon}{\epsilon_\mathrm{w} + 2\epsilon} + \nu_d \frac{\epsilon_\mathrm{d} - \epsilon}{\epsilon_\mathrm{d} + 2\epsilon} = 0, \tag{10}$$

where ϵ_w and ϵ_d are the permittivities and ν_w and ν_d are the volume fractions of the water and dry components, respectively. The Bruggeman model rests on the assumption that the components of the mixture can be treated as spherical inclusions in a homogenous background. An external electric field $\mathbf{E_0}$ applied far from one inclusion, illustrated in Figure 7, will lead to a dipole moment around the inclusion. The polarization from this dipole forces a deviation from $\mathbf{E_0}$. The polarization summed over both types of inclusions must vanish, and this constraint is represented by equation (10). This model can be extended to three components by modelling the permittivity of the dry component as another Bruggeman mixture of air and fibre. The resulting model simplifies to

$$\nu_w \frac{\epsilon_\mathrm{w} - \epsilon}{\epsilon_\mathrm{w} + 2\epsilon} + \nu_a \frac{\epsilon_\mathrm{a} - \epsilon}{\epsilon_\mathrm{a} + 2\epsilon} + \nu_f \frac{\epsilon_\mathrm{f} - \epsilon}{\epsilon_\mathrm{f} + 2\epsilon} = 0. \tag{11}$$

This equation does not have a simple analytic solution and must be solved numerically for each frequency component of the permittivity.

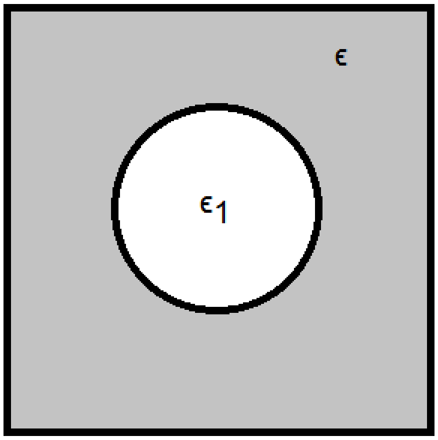

Figure 7 – Illustration of the Bruggeman effective medium theory approximating a binary composite material as a spherical inclusion in a homogenous dielectric.

A different effective medium theory, proposed by Landau, Lifshitz, and Looyenga (LLL), was used by Jördens et. al. to model the moisture content of a leaf [14]. It rests on the assumption that the permittivity of each component ϵ_i is similar to the rest ($|\epsilon_i - \epsilon| \ll \epsilon$) [15]. As Figure 8 shows, this inequality holds weakly for fibre and air and is violated for water at all frequencies in our bandwidth. Nonetheless, as I will show later in this chapter, the LLL model reproduces the results of the Bruggeman model for the terahertz properties of paper. Furthermore, in Section 4.4 I show that the LLL model is consistent with our experimental results on paper. Consequently, as a practical matter, we will work with the LLL model, even though the assumptions from which it is derived are not valid.

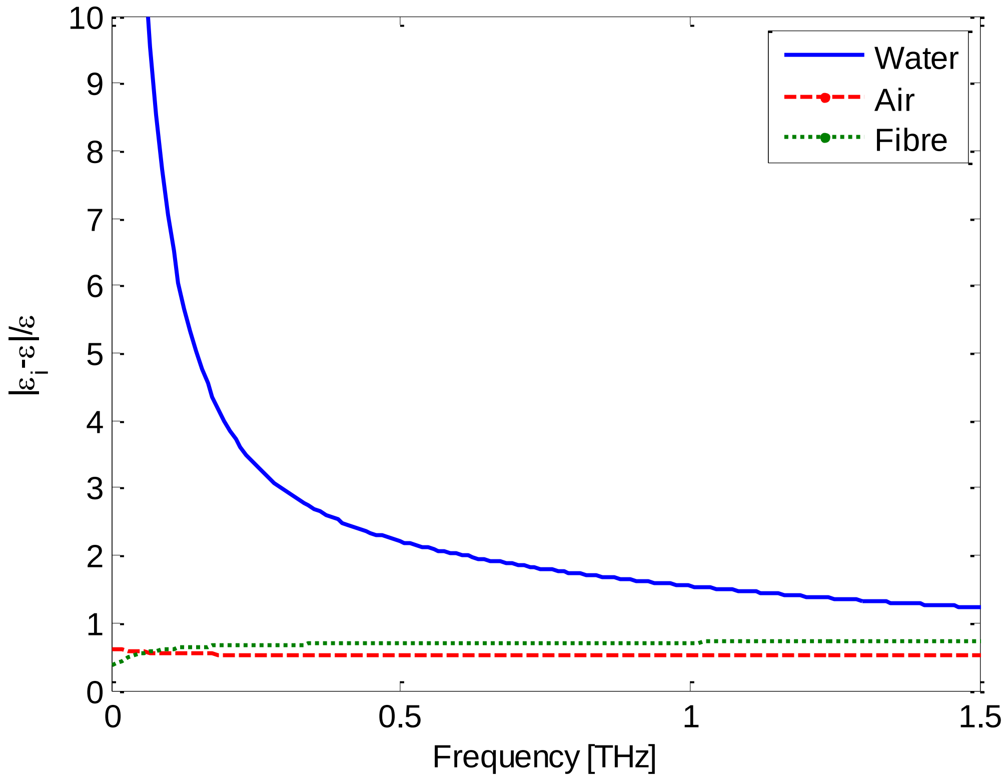

Figure 8 – Plot of the difference in permittivity between the components and the mixture, normalized by the mixture. The derivation for the LLL model assumes that this value is much less than one, a condition that is not well satisfied.

The derivation from Landau and Lifshitz proceeds as follows [15]. For a local electric field of $\mathbf{E} = \bar{\mathbf{E}} + \delta\mathbf{E}$, and a local permittivity of $\bar{\epsilon} + \delta\epsilon$, where $\bar{\epsilon}$ is the volume averaged permittivity, equation (9) becomes

$$\frac{\bar{\mathbf{D}}}{\epsilon_0} = \overline{\left(\bar{\epsilon} + \delta\epsilon\right)(\bar{\mathbf{E}} + \delta\mathbf{E})} = \bar{\epsilon}\bar{\mathbf{E}} + \overline{\delta\epsilon\delta\mathbf{E}}\,, \tag{12}$$

since the volume averages of $\delta\boldsymbol{E}$ and $\delta\epsilon$ are zero. The zeroth order approximation of the $\overline{\delta\epsilon\delta\boldsymbol{E}}$ term in this equation yields $\epsilon = \bar{\epsilon}$, a linear average of the components.

To differentiate between two components with real permittivities, a higher order expansion is necessary. The next higher order term is determined by averaging over a volume of constant $\delta\epsilon$. Since the mixture is assumed to be isotropic, the derivative of $\delta\boldsymbol{E}$ along any axis x_i is related to the vector divergence,

$$\frac{\partial}{\partial x_i}\overline{\delta E_i} = \frac{1}{3}\nabla \bullet \overline{\delta\mathbf{E}} \tag{13}$$

By taking the divergence of equation (12), noting that $\nabla \bullet \boldsymbol{D} = 0$, and neglecting higher order terms, we get

$$\nabla \bullet \left(\left(\bar{\epsilon} + \delta\epsilon\right)\left(\bar{\mathbf{E}} + \delta\mathbf{E}\right)\right) = \bar{\epsilon}\nabla \bullet \delta\mathbf{E} + \bar{\mathbf{E}}\nabla\delta\epsilon = 0\,. \tag{14}$$

With equation (13), this gives

$$\begin{gathered} 3\bar{\epsilon}\,\frac{\partial}{\partial x_i}\overline{\partial E_i} = -\overline{E_i}\,\frac{\partial\delta\epsilon}{\partial x_i}, \text{ or} \\ \overline{\delta E_i} = -\frac{\overline{E_i}}{3\bar{\epsilon}}\delta\epsilon, \end{gathered} \tag{15}$$

for any axis x_i. Since the choice of axis is arbitrary, equation (15) can be expressed in vector form

$$\overline{\delta\mathbf{E}} = -\frac{\bar{\mathbf{E}}}{3\bar{\epsilon}}\delta\epsilon\,. \tag{16}$$

Multiplying both sides of this equation by $\delta\epsilon$ and performing the volume average over the rest of the components gives

$$\overline{\delta\epsilon\delta\mathbf{E}} = -\left(\frac{1}{3\bar{\epsilon}}\right)\bar{\mathbf{E}}\overline{(\delta\epsilon)^2} \tag{17}$$

Substituting this result into equation (12) yields

$$\epsilon = \bar{\epsilon} - \frac{\overline{(\delta\epsilon)^2}}{3\bar{\epsilon}}, \tag{18}$$

which to second order in $\delta\epsilon$, can be written as

$$\sqrt[3]{\epsilon} = \overline{\sqrt[3]{\epsilon}}, \tag{19}$$

by using

$$\overline{\sqrt[3]{\epsilon}} = \overline{\sqrt[3]{\bar{\epsilon} + \delta\epsilon}} \approx \sqrt[3]{\bar{\epsilon}}\left(1 - \frac{\overline{(\delta\epsilon)^2}}{9\bar{\epsilon}^2}\right). \tag{20}$$

Equation (19) tells us that the cube root of the effective permittivity of a mixture is linear average of the cube roots of the constituent permittivities. Since this derivation did not specify the number of constituent components, for a mixture of *N* components, with fractional volumes v_i and permittivities ϵ_i, the effective permittivity will be

$$\sqrt[3]{\epsilon} = \sum_{\mathrm{i}=1}^{\mathrm{N}} v_i \sqrt[3]{\epsilon_{\mathrm{i}}}. \tag{21}$$

The sum of the volume fractions must equal 1. This model for the relative permittivity can be related to the refractive index and absorption coefficient through

$$\sqrt{\epsilon} = n + i\frac{\alpha c}{2\omega}. \tag{22}$$

Figure 9 shows a comparison between the LLL model and the Bruggeman model as a function of fibre volume fraction for three different frequencies. The vertical axis shows the relative difference between the permittivities given by the two models, calculated for a constant water fraction of 5%. The models agree to within 2-3% at high frequencies, but diverge by as much as 10% at low frequencies.

This convergence at high frequencies suggests that despite the different assumptions that went into each derivation, either model may be used to approximate the physical response of paper. By limiting my analysis to higher frequency components, the difference between the models is small. Finally, Looyenga showed that under certain assumptions the Bruggeman model could be derived from the LLL model and that it reproduces experimental results for glass spheres immersed in carbon tetrachloride more closely than other models [16]. Therefore, I used the LLL model to calculate permittivities, as it is computationally faster than the Bruggeman model.

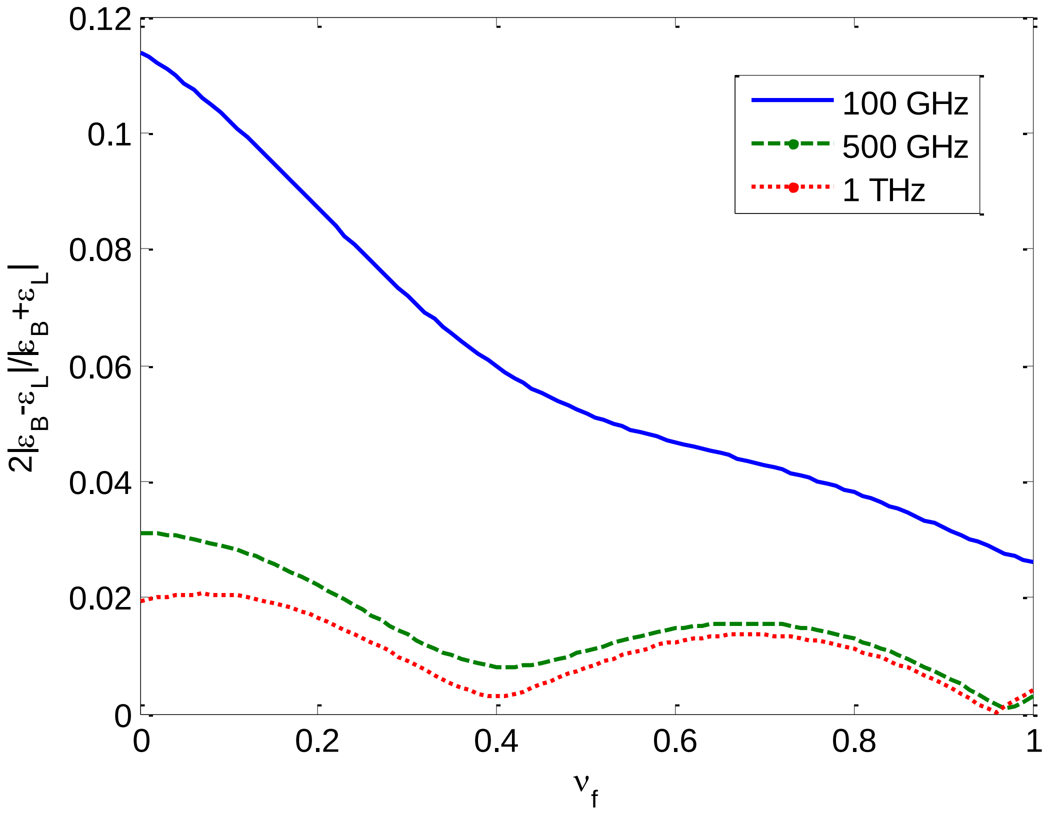

Figure 9 – Comparison of Bruggeman and Landau, Lifshitz, and Looyenga effective medium theories. The difference between the Bruggeman permittivity ϵ_B and the LLL permittivity ϵ_L is normalized by the average of the two and plotted against fibre volume fraction for three frequencies. Models agree closest at higher frequencies.

3.1.1 The effective medium theory for paper

Mousavi et. al. showed that a two-component effective medium theory can be used to determine the thickness and moisture content of paper [7]. Their model divides paper into water and dry components. The dry component is comprised of air and a solid portion consisting primarily of fibre and ash. Neglecting the mass of the air in the mixture, the basis weight can be calculated directly from the densities of water and fibre, the volume fractions of water and fibre in the paper, and the paper thickness. I therefore chose to model paper as a mixture of water, air, and fibre.

For these three components, equation (21) becomes

$$\sqrt[3]{\epsilon} = \nu_a \sqrt[3]{\epsilon_a} + \nu_f \sqrt[3]{\epsilon_f} + \nu_w \sqrt[3]{\epsilon_w}\,, \tag{23}$$

with air, fibre, and water volume fractions ν_a, ν_f, and ν_w, and permittivities ϵ_a, ϵ_f, and ϵ_w, respectively, with the constraint $\nu_a + \nu_f + \nu_w = 1$. This model is similar to the one that Jördens et. al. used to successfully model a leaf [14].

The permittivity of air is approximately one, and I chose the fibre permittivity to be a constant, consistent with the dry paper measurements of Mousavi et. al. [7]. The fibre permittivity is determined experimentally and is expected to vary for different paper compositions. For this work I chose $n_f = 1.88$.

A simple yet accurate model of water's interaction in the terahertz regime is given by the double Debye model [17]

$$\epsilon_\mathrm{w} = \epsilon_\infty + \frac{\epsilon_\mathrm{s} - \epsilon_1}{1 + i\omega\tau_1} + \frac{\epsilon_1 - \epsilon_\infty}{1 + i\omega\tau_2}\,, \tag{24}$$

with experimentally determined constants as listed in Table 1 [18]. The two Debye relaxation times τ_1 and τ_2 are associated with translational and rotational diffusion, and hydrogen bond and structural rearrangements [19].

Table 1 – Parameters used in the Double-Debye model for the permittivity of water [18].

ϵ_∞	ϵ_S	ϵ_1	τ_1 [ps]	τ_2 [ps]
3.216	79.4838	5.2523	8.1078	0.1778

In the next chapter, I provide evidence for an additional loss mechanism related to Rayleigh scattering. This scattering causes an absorption that can be added to the overall absorption from equation (23). Jördens et. al. proposed this mechanism in their study of the terahertz properties of leaves and associated it with surface scattering [14]. Jördens et. al. did not consider bulk scattering which may also be important; future work will be required to determine the origin of scattering in paper.

The microstructure of paper has dimensions that are much smaller than our 100 μm characteristic wavelength, and it is therefore appropriate to consider it in the Rayleigh scattering regime. The intensity of Rayleigh scattering scales as $1/\lambda^4$, so the electric field scales as $1/\lambda^2$. Assuming that the dominant effect was surface scattering, the effective absorption of a sample of thickness d is [14]

$$\alpha_{scat} = \left((n-1)\frac{4\pi\tau}{\lambda} \right)^2 \frac{1}{d}, \tag{25}$$

where τ is a length parameter related to the roughness and n is the real part of the refractive index of the paper, calculated from the effective medium theory. The $1/d$ term accounts for the thickness independence of the absorption. Jördens et. al. include the $(n-1)^2$ term to account for the difference in polarizability between air and paper. If bulk scattering plays the dominant role, τ will instead relate to the size of the fibres and the scattering efficiency should be independent of thickness. Moreover, we would expect bulk scattering to depend on the $\chi = \epsilon - 1$ rather than the n – 1 term in equation (25).

I assumed that the total absorption can be written as

$$\alpha = \alpha_{scat} + \alpha_{pap}. \tag{26}$$

With this absorption and the refractive index from the LLL model, equation (23), the response function of paper can be determined from equation (6). Figure 10 summarizes the entire model, from the permittivity assumptions to the complete transfer function.

The three volume fractions can be related to the paper processing parameters – caliper, basis weight and moisture content – through simple relations

$$\begin{gathered} \mathrm{M} = \frac{v_w \rho_w}{v_w \rho_w + v_f \rho_f} \text{ and} \\ \mathrm{BW} = (v_w \rho_w + v_f \rho_f) d, \end{gathered} \tag{27}$$

with $\rho_w = 1.0\ \mathrm{kg/m^3}$ and $\rho_f = 1.5\ \mathrm{kg/m^3}$ the mass densities of water and fibre, respectively.

The permittivity is dependent on only two free parameters, since the sum of the three volume fractions is one. To account for this constraint, I defined angular coordinates such that

$$\begin{gathered} \cos^2\phi = v_w, \\ \sin^2\phi \cos^2\theta = v_a, \text{ and} \\ \sin^2\phi \sin^2\theta = v_f, \end{gathered} \tag{28}$$

with ϕ and θ bounded between 0 and $\pi/2$ to ensure that the volume fractions are non-negative. As Figure 11 shows, this formulation restricts the fit to the surface of one quadrant of the unit sphere in v_w, v_a, and v_f, and therefore automatically satisfies the volume fraction constraint.

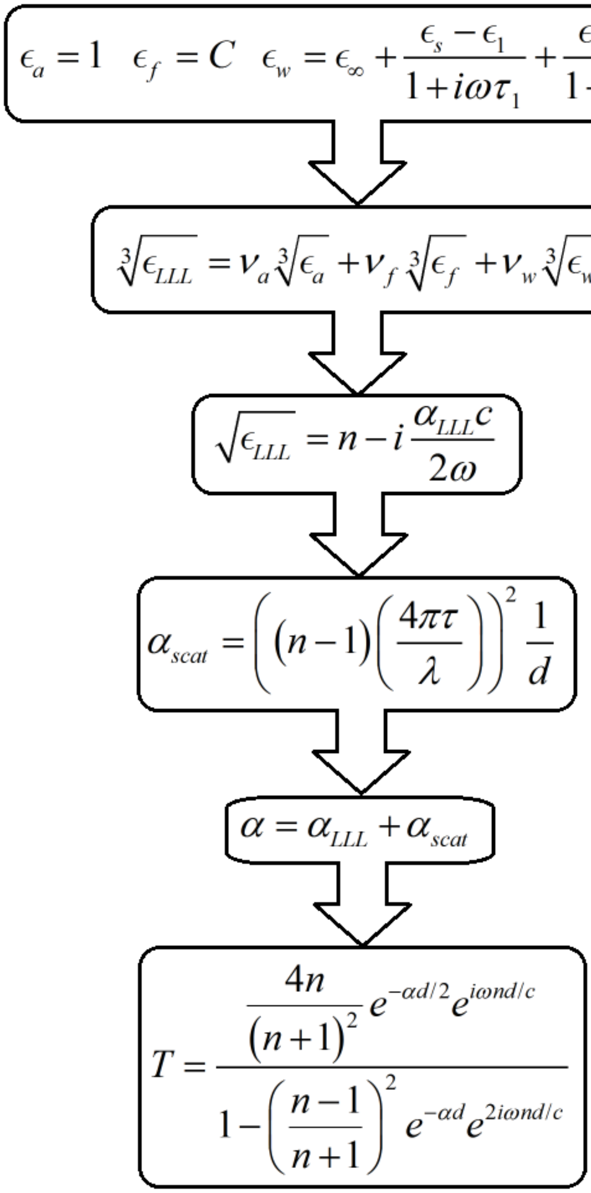

$$\epsilon_a = 1 \quad \epsilon_f = C \quad \epsilon_w = \epsilon_\infty + \frac{\epsilon_s - \epsilon_1}{1+i\omega\tau_1} + \frac{\epsilon_1 - \epsilon_\infty}{1+i\omega\tau_2}$$

$$\sqrt[3]{\epsilon_{LLL}} = \nu_a \sqrt[3]{\epsilon_a} + \nu_f \sqrt[3]{\epsilon_f} + \nu_w \sqrt[3]{\epsilon_w}$$

$$\sqrt{\epsilon_{LLL}} = n - i\frac{\alpha_{LLL} c}{2\omega}$$

$$\alpha_{scat} = \left((n-1)\left(\frac{4\pi\tau}{\lambda}\right)\right)^2 \frac{1}{d}$$

$$\alpha = \alpha_{LLL} + \alpha_{scat}$$

$$T = \frac{\frac{4n}{(n+1)^2} e^{-\alpha d/2} e^{i\omega n d/c}}{1 - \left(\frac{n-1}{n+1}\right)^2 e^{-\alpha d} e^{2i\omega n d/c}}$$

Figure 10 – Summary of the three-component model for paper. Using models for the permittivities of air, fibre, and water, I calculate an effective permittivity for paper. This permittivity relates to the absorption and refractive index. An additional absorption is added to account for scattering effects. Finally, the index and total absorption are used to calculate the transfer function. Experimental data is used to estimate ϵ_f and τ; ν_f, ν_a, ν_w, and d are estimated; and the rest of the parameters are modelled.

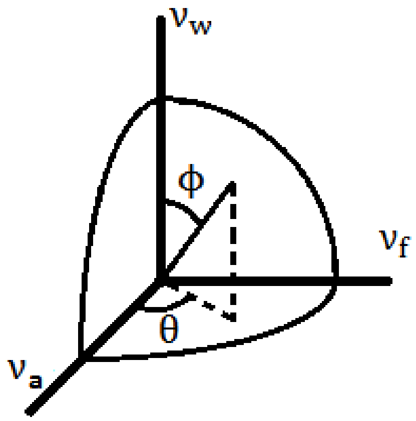

Figure 11 – Illustration of spherical coordinate transform. The radius of this partial sphere is one. The angles ϕ and θ are bounded between 0 and π/2. Allowed solutions are constrained to the section of the unit sphere shown.

3.2 Monte Carlo simulations to determine parameter uncertainties

To investigate the behaviour of this model, I performed Monte Carlo simulations. These simulations were designed to mimic our experimental apparatus and available samples. Strong correlations between the model parameters are observed and discussed.

3.2.1 Simulation process and parameters

The Monte Carlo simulations were performed in MATLAB with an idealized terahertz pulse

$$E_i(t) = \left(1 - 2\left(\frac{t - t_0}{w}\right)^2\right) e^{-(t-t_0)^2/w^2}, \tag{29}$$

with pulse width w and peak position t_0. This pulse was chosen as it best replicates the temporal and spectral characteristics of our spectrometer, as seen in Figure 12. I chose realistic pulse and paper parameters, summarized in Table 2, for our experimental setup. The signal-to-noise ratio (SNR) of 350, defined in Figure 13 as the peak spectral amplitude divided by the mean of the high-frequency noise floor, is relatively low but realistic for high scan rate applications. The fibre index n_f and scattering parameter τ are chosen based on the experimental results for the paper samples discussed in Section 4.4.

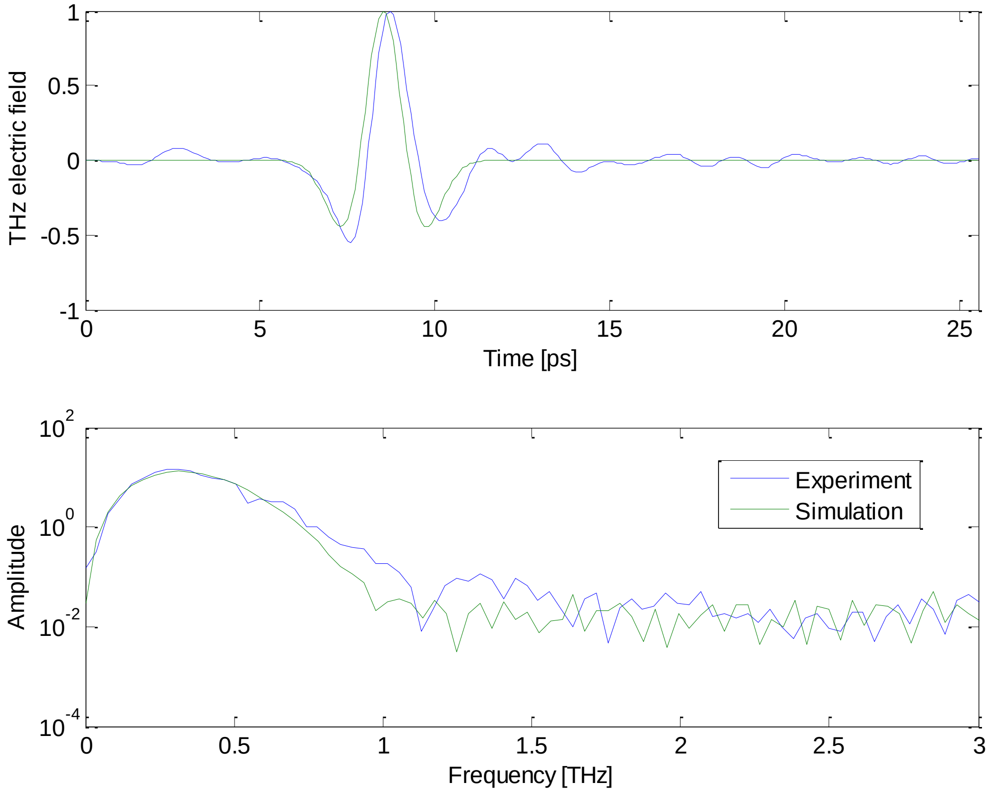

Figure 12 – Comparison of experimental (blue) and simulated (green) reference pulses. Table 2 lists the parameters used for the simulated pulse.

Table 2 – Parameters used in Monte Carlo simulations.

Simulation Parameter	**Symbol**	**Value**
Number of MC runs	N_{MC}	100
Number of data points	N	256
Sampling period	T_0	0.1 ps
Pulse width	w	1 ps
Peak position	t_0	8.53 ps
Signal-to-noise ratio	SNR	350
Fibre index	n_f	1.88
Scattering parameter	τ	10 µm

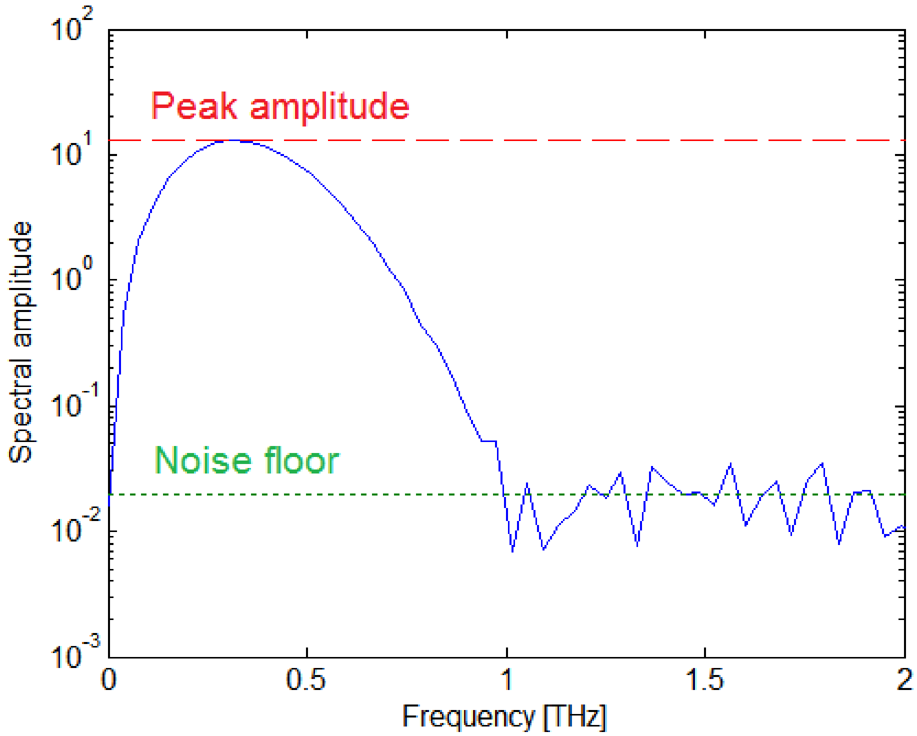

Figure 13 – Frequency-dependent definition of the signal-to-noise ratio (SNR). The SNR is the peak spectral amplitude (red) divided by the mean of the high-frequency noise, also known as the noise floor (green).

An ideal sample pulse is generated by applying the transfer function given by equation (6) to the ideal pulse $E_i(t)$. The transfer function is specified by a set of ideal process parameters: caliper, basis weight, and moisture content, given by the parameter vector θ_{id}.

I add Gaussian white noise (GWN) to the ideal sample pulse in the time-domain $E_s(t)$ with a standard deviation given by

$$\sigma_{GWN} = \frac{1}{2 \bullet SNR}. \tag{30}$$

A reference pulse $E_r(t)$ is generated by a shifting a second ideal pulse by equation (8), and adding an equal amount of Gaussian white noise.

I use the maximum likelihood method to determine the unknown parameters in this model, minimizing the cost function [20]

$$C(\theta)=\frac{1}{2}\sum\frac{\left|\mathbf{E}_s(\omega)-\mathbf{T}(\omega,\theta)\mathbf{E}_r(\omega)\right|^2}{\sigma_s^2+\left|\mathbf{T}(\omega,\theta)\right|^2\sigma_r^2}, \tag{31}$$

with respect to the parameter vector θ. The experimental inputs to this equation are $E_s(\omega)$ and $E_r(\omega)$, the Fourier transforms of the simulated sample and reference pulses; $T(\omega,\theta)$, the frequency-dependent transfer function, given by equation (8); and σ_s and σ_r, the measured standard deviations of the Gaussian white noise on each pulse. The fits are performed over the frequency interval of highest SNR in our spectrometer: 300 GHz to 1.1 THz. The entire simulation process is summarized in Figure 14.

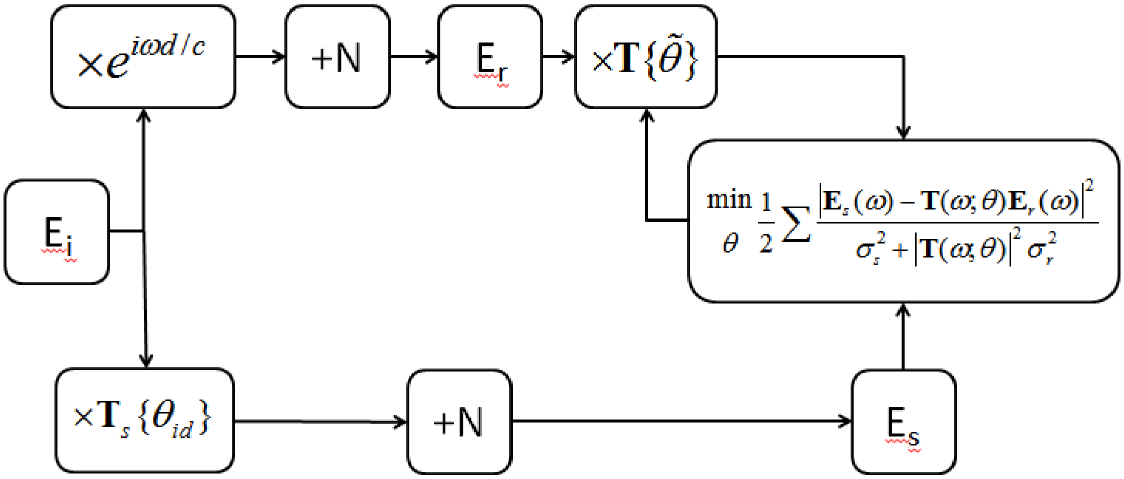

Figure 14 - Process flow for Monte Carlo simulations. In the bottom branch, a sample pulse E_s is generated by adding noise (N) to an ideal pulse E_i that has passed through a simulated ideal sample with parameters θ_{id}. Noise is added to a shifted ideal pulse in the top branch to get the reference pulse E_r. Parameter estimates of the transfer function are obtained by minimizing the maximum likelihood estimator (MLE) with respect to the free parameters θ. The standard deviations of the Gaussian white noise on the reference and sample pulses σ_s and σ_r respectively are input to the MLE.

While typical paper products are about 100 μm thick with basis weights of about 100 gsm, for the following simulations I chose paper parameters in the trange of the samples measured in the next chapter. I chose basis weights of 500, 750 and 1000 gsm; moisture contents of 2, 5, and 7%; and thicknesses of 750, 1000, and 1500 μm. Each combination of parameters was simulated with 100 Monte Carlo sample and reference pulses. A final sample with parameters more typical for commercial paper was also simulated, with 100 μm thickness, 5% moisture content, and a basis weight of 75 gsm.

3.2.2 Physical parameter results

Figure 15 shows the volume fraction and thickness estimates from samples with a basis weight of 750 gsm, moisture content of 5%, and thicknesses of 750, 1000, and 1500 μm. The solid curves show the dependence of the volume fractions on thickness for the chosen ideal moisture content and basis weight. For a fixed moisture content and basis weight, a change in thickness relates to a change in density, since basis weight is the product of density and thickness.

Figure 16 shows a plot of the air and fibre volume fraction estimates for the 750, 1000, and 1500 μm thicknesses and Figure 17 shows just the 1000 μm sample. From these two plots, it is apparent that there is a strong correlation between the air and fibre components of the sample. The inset of Figure 17 shows that the sum of the two components, $v_a + v_f$, gives a more precise estimate than the difference, $v_a - v_f$, and that these two terms are less correlated than the air and fibre volume fractions.

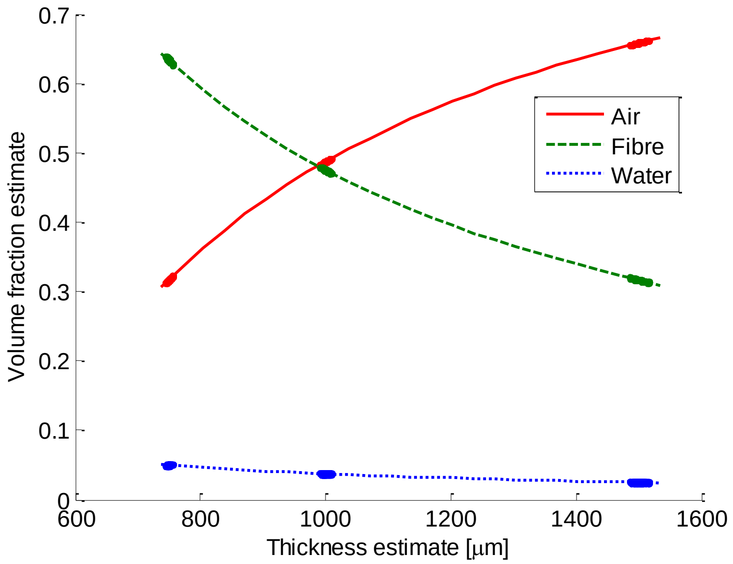

Figure 15 – Volume fraction versus thickness estimates for Monte Carlo simulations. Markers show air (red), fibre (green), and water (blue) volume fraction estimates for simulations with ideal thicknesses of 750, 1000, and 1500 μm. Solid curves show the ideal volume fractions relationships over all thicknesses for constant moisture content (5%) and basis weight (750 gsm).

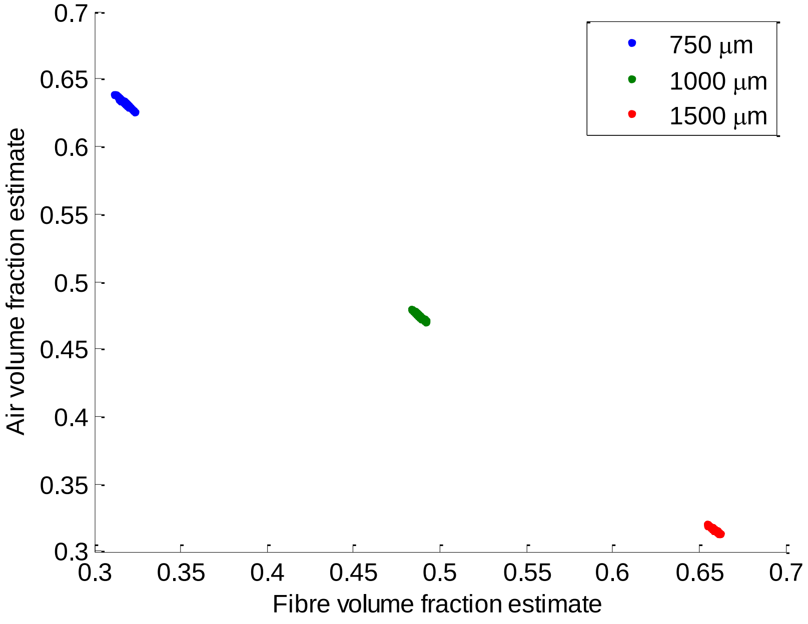

Figure 16 – Air versus fibre volume fraction estimates for Monte Carlo simulations. Results are plotted for 750 (blue), 1000 (green), and 1500 μm (red) thick paper samples with constant moisture content (5%) and basis weight (750 gsm). The plot shows strong correlation between these two parameters.

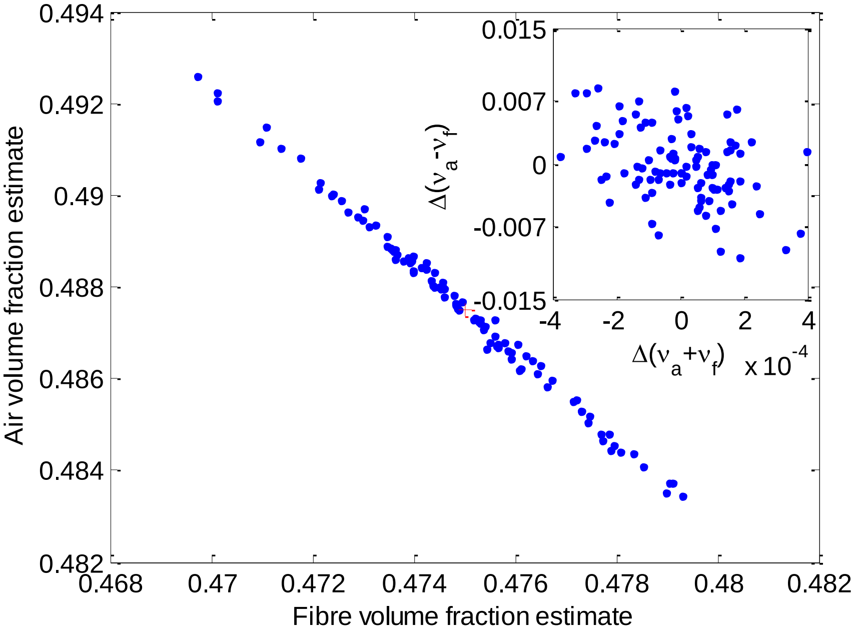

Figure 17 – Air versus fibre volume fraction estimates for Monte Carlo simulations of 1000 μm thick paper with 750 gsm basis weight and 5% moisture content. Inset shows the difference versus the sum of the air and fibre volume fractions, centred on the expected values.

3.2.3 Understanding the correlations

The correlation between the fibre and air volume indicates that the model distinguishes between water and dry content much better than it discriminates between the dry content constituents. This is related to the dispersion of each component. At a single frequency terahertz spectroscopy measures the optical path length $OPL = n\ d$.[3] For a small change in index δn and thickness δd, the new optical path length will be

$$OPL = \left(n + \delta n\right)\left(d + \delta d\right) = nd + n\delta d + d\delta n + \delta d \delta n. \tag{32}$$

Therefore, to first order, for correlated changes $\delta n = -(n/d)\delta d$, the optical path length From equation (23), the refractive index of a dry sample increases with density, since the permittivity of fibre is greater than that of air. Therefore, the refractive index will increase with decreasing thickness, leaving the optical path length approximately constant.

To demonstrate this point we may rewrite the LLL model in terms of $p = v_a + v_f$ and $m = v_a - v_f$,

$$\sqrt[3]{\epsilon} = \sqrt[3]{\epsilon_w} + \frac{p}{2}\left(\sqrt[3]{\epsilon_a} + \sqrt[3]{\epsilon_f} - 2\sqrt[3]{\epsilon_w}\right) + \frac{m}{2}\left(\sqrt[3]{\epsilon_a} - \sqrt[3]{\epsilon_f}\right). \tag{33}$$

From these three terms, we can see the origin of the correlations more clearly. We can ignore the first term since it is independent of *p* and *m*. The second term is large, complex, and frequency-dependent, while the final term is small, real, and constant with frequency. This suggests that the ability to differentiate the fibre and air volume fractions is dependent on the difference between the fibre and air permittivity. Since these values are relatively similar, it is difficult to obtain a good estimate of *m*, while *p* is easier to obtain. From equation (32) we can see that $d\delta n$ will have three separate contributions, one from each term in equation (33). This allows us to determine *d*, $d\delta p$, and $d\delta m$, which will not be compensated by $n\delta d$ at all frequencies.

---

[3] Optical path length is defined for a homogenous medium. In general $OPL = \int n(x)dx$.

If equation (33) adequately explains this correlation and its limits, we should expect that as the fibre index increases, the *m* term will be easier to determine and therefore the standard deviation of its estimate will decrease. The Jacobian

$$J = \begin{pmatrix} \frac{\partial C(\omega_1)}{\partial d} & \frac{\partial C(\omega_1)}{\partial \phi} & \frac{\partial C(\omega_1)}{\partial \theta} \\ \vdots & \vdots & \vdots \\ \frac{\partial C(\omega_n)}{\partial d} & \frac{\partial C(\omega_n)}{\partial \phi} & \frac{\partial C(\omega_n)}{\partial \theta} \end{pmatrix} \tag{34}$$

for this system is defined in terms of the partial derivatives of the cost function with respect to the estimated variables $\{d, \phi, \theta\}$, at each frequency. The Jacobian is calculated numerically as part of the fit algorithm and is used to find the covariance matrix by

$$V_{d\phi\theta} \equiv \begin{pmatrix} \sigma_d^2 & \sigma_{d\phi} & \sigma_{d\theta} \\ \sigma_{d\phi} & \sigma_\phi^2 & \sigma_{\phi\theta} \\ \sigma_{d\theta} & \sigma_{\phi\theta} & \sigma_\theta^2 \end{pmatrix} = \left(J^T J\right)^{-1}. \tag{35}$$

To relate this to uncertainties in the variables *d, p,* and *m*, we define the transformation matrix

$$G \equiv \begin{pmatrix} \frac{\partial d}{\partial d} & \frac{\partial d}{\partial \phi} & \frac{\partial d}{\partial \theta} \\ \frac{\partial p}{\partial d} & \frac{\partial p}{\partial \phi} & \frac{\partial p}{\partial \theta} \\ \frac{\partial m}{\partial d} & \frac{\partial m}{\partial \phi} & \frac{\partial m}{\partial \theta} \end{pmatrix} = \begin{pmatrix} 1 & 0 & 0 \\ 0 & \sin(2\phi) & 0 \\ 0 & \cos(2\phi)\sin(2\theta) & -2\sin^2(\phi)\sin(2\theta) \end{pmatrix}. \tag{36}$$

When this is evaluated at the mean values of *d*, *ϕ*, and *θ*, the covariance matrix V_{dpm} is

$$V_{dpm} = G V_{d\phi\theta} G^T. \tag{37}$$

Figure 18 shows a plot of the variances, σ_p^2 and σ_m^2, versus fibre index, for a 1000 μm thick sample with basis weight of 750 gsm and moisture content of 5%. All three parameters, *d*, *ϕ*, and *θ*, were allowed to vary. These results agree with the predicted behaviour of equation (33), as the coefficients of both terms increase with fibre index.

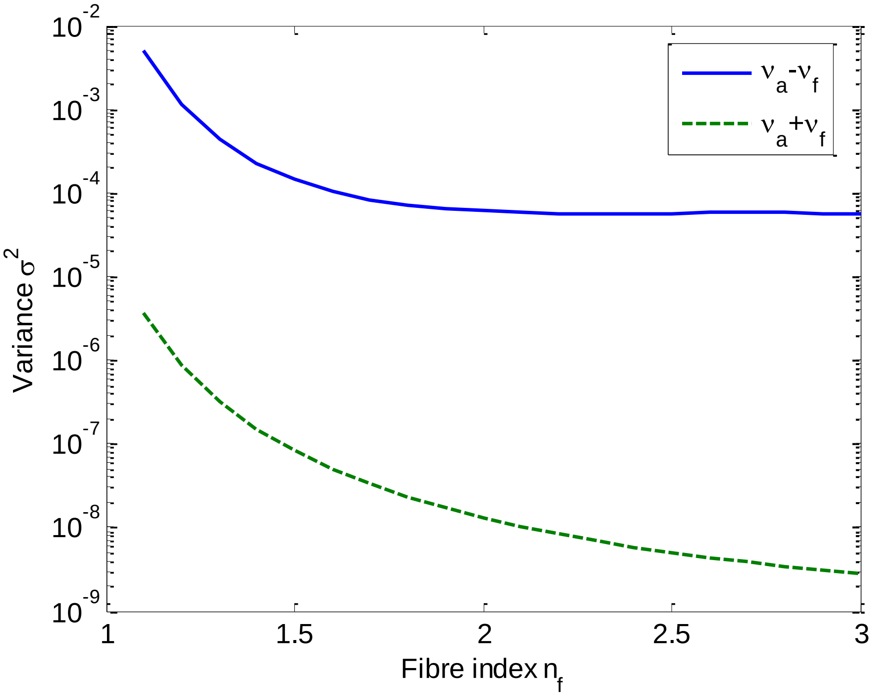

Figure 18 – Variance of ν_f+ν_a (green dashes) and ν_a-ν_f (blue line) versus fibre index.

Alternatively, we can understand this phenomenon in terms of the optical transfer function given by equation (8). We need to extract the index *n*, absorption *α*, and thickness *d*, which appear in the transfer function as *n·d* and *α·d* in the dominant exponential terms and *n* in the relatively weak pre-factor. Since we are able to measure the magnitude and phase of the transfer function as a function of frequency, we have two known functions to specify a frequency-dependent function with three unknown parameters. As the absorption is frequency-dependent, the estimate of *α·d* is the most precise, since it relates closest to water's complex and frequency-dependent permittivity. Because of the constraint $\nu_a + \nu_f + \nu_w = 1$, the precise estimate of ν_w corresponds to a precise estimate of $\nu_a + \nu_f$. The thickness estimate can then be found from both *α·d* and *n·d*. The remaining frequency dependence of the index is then accounted for with the difference in the air and fibre volume fractions v_a - v_f, which are similar enough to result in strong correlations. In the next chapter, this model is shown to qualitatively agree with the data.

3.2.4 Process parameter results

Figure 19 shows the simulation results in terms of the three optical parameters and the corresponding paper process parameters for the 1000 µm sample, calculated using equation (27).

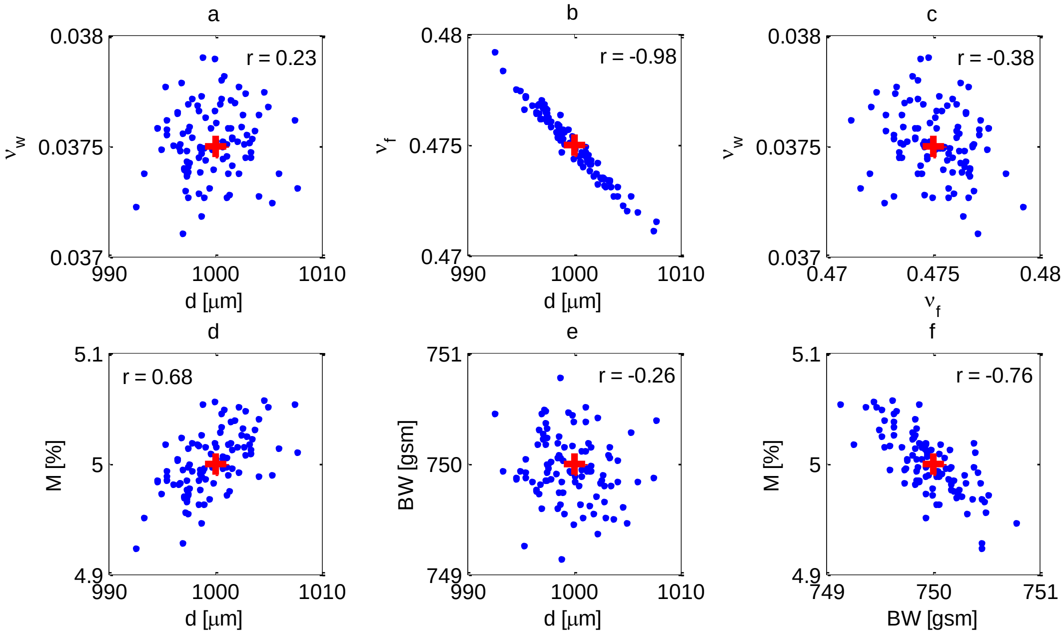

Figure 19 – Corresponding optical (top row, a-c) and paper process (bottom row, d-f) parameter estimates from Monte Carlo simulations for a 1000 µm sample with 5% moisture content and a basis weight of 750 gsm. Correlation coefficients are inset. Red crosses show expected values.

The relationships between Figure 19 a-c and Figure 19 d-f can be understood by considering the propagation of uncertainties and covariance. From equation (27) the transformation from the model parameters $\{d, v_w, v_f\}$ to the process parameters $\{d, M, BW\}$ is

$$G=\begin{pmatrix} \dfrac{\partial d}{\partial d} & \dfrac{\partial d}{\partial \nu_w} & \dfrac{\partial d}{\partial \nu_f} \\ \dfrac{\partial M}{\partial d} & \dfrac{\partial M}{\partial \nu_w} & \dfrac{\partial M}{\partial \nu_f} \\ \dfrac{\partial BW}{\partial d} & \dfrac{\partial BW}{\partial \nu_w} & \dfrac{\partial BW}{\partial \nu_f} \end{pmatrix} = \begin{pmatrix} 1 & 0 & 0 \\ 0 & \dfrac{\nu_f \rho_f \rho_w}{(\nu_f \rho_f + \nu_w \rho_w)^2} & \dfrac{-\nu_w \rho_f \rho_w}{(\nu_f \rho_f + \nu_w \rho_w)^2} \\ \nu_f \rho_f + \nu_w \rho_w & d\rho_w & d\rho_f \end{pmatrix}. \quad (38)$$

For 1000 µm thick paper, 750 gsm basis weight, and 5% moisture content the matrix reduces to

$$\mathrm{G}=\begin{pmatrix} 1 & 0 & 0 \\ 0 & 1.60 & -0.126 \\ 5.11 & 0.00872 & 0.0101 \end{pmatrix}. \quad (39)$$

The covariance matrix transform is therefore

$$V_{d\,M\,BW} = G V_{d\nu_w\nu_f} G^T . \quad (40)$$

From Figure 19 (a), the nearly isotropic distribution tells us that σ_{dw} is small; from Figure 19 (b) σ_{df} is large and negative; and from Figure 19 (c) σ_{fw} is small. The respective correlation coefficients $r_{xy} \equiv \sigma_{xy} / \left(\sigma_x \sigma_y\right)$ are $r_{dw} = 0.23$, $r_{df} = -0.98$, and $r_{fw} = -0.38$. The covariance matrix is

$$V_{d\nu_w\nu_f} = \begin{pmatrix} \sigma_d^2 & \sigma_{dw} & \sigma_{df} \\ \sigma_{dw} & \sigma_w^2 & \sigma_{wf} \\ \sigma_{df} & \sigma_{wf} & \sigma_f^2 \end{pmatrix} = \begin{pmatrix} 1.2\times10^{-11} & 7.4\times10^{-11} & -6.0\times10^{-9} \\ 7.4\times10^{-11} & 2.0\times10^{-8} & -7.11\times10^{-8} \\ -6.0\times10^{-9} & -7.11\times10^{-8} & 3.2\times10^{-6} \end{pmatrix}, \quad (41)$$

which leads to the dominant terms of $V_{d\,M\,BW}$ given in Table 3. We therefore expect $\sigma_{d\,M}$ to be positive, $\sigma_{d\,BW}$ to be near zero, and $\sigma_{M\,BW}$ to be negative, as observed.

Table 3 – Terms of the *{d,M,BW}* covariance matrix defined in relation to the *{d,ν_w,ν_f}* covariance matrix.

Matrix Element	**Dominant terms**
$\sigma_{d\,M}$	$1.6\sigma_{dw}-0.13\sigma_{df}$
$\sigma_{d\,BW}$	$5.1\sigma_d^2+0.01\sigma_{df}$
$\sigma_{M\,BW}$	$-0.0013\sigma_f^2+0.015\sigma_{wf}$

Table 4 summarizes the results of Monte Carlo simulations for different caliper, basis weights, and moisture contents. The first row of the table gives an estimate for standard copy paper, while the remaining rows are representative of the samples tested experimentally in the next chapter.

These results suggest that caliper precisions of better than 1% should be possible. The basis weight is also estimated quite precisely, 0.5 gsm in the worst scenarios. Estimates for the moisture content are all consistently within 1% of the ideal value, except for the 100 μm sample, which has a large error that may be due to the relatively small amount of water present. The basis weight estimates are fairly independent of the sample's properties, while the precision of the thickness estimate decreases for thin and dry samples.

Table 4 – Monte Carlo simulation results for different ideal thicknesses, basis weight, and moisture contents (first three columns), and the mean (indicated by a bar) and standard deviation (σ) of the estimates for 100 simulations.

Ideal parameter			**Simulation results**					
d	**BW**	**M**	$\bar{d}$	σ_d	$\overline{BW}$	σ_{BW}	$\bar{M}$	σ_M
μm	**gsm**	**% mass**	**μm**	**μm**	**gsm**	**gsm**	**% mass**	**% mass**
100	75	5	100.1	0.7	74.9	0.5	5.1	0.5
750	500	2	750	3	500.0	0.3	2.00	0.05
750	500	5	750	4	500.0	0.4	5.00	0.06
750	500	7	750	4	500.0	0.4	7.01	0.07
750	750	2	750	2	750.0	0.3	2.00	0.03
750	750	5	750	2	750.0	0.4	5.00	0.04
750	750	7	750	3	750.1	0.5	6.99	0.06
1000	500	2	1000	4	500.0	0.3	2.00	0.03
1000	500	5	1000	5	500.0	0.3	5.00	0.04
1000	500	7	1000	6	500.0	0.3	7.00	0.04
1000	750	2	1000	3	750.0	0.3	2.00	0.03
1000	750	5	1001	4	750.0	0.3	5.00	0.04
1000	750	7	1000	5	750.1	0.3	7.00	0.05
1500	500	2	1500	9	500.0	0.3	2.00	0.03
1500	500	5	1502	10	500.0	0.3	5.00	0.03
1500	500	7	1501	13	500.0	0.3	7.00	0.04
1500	750	2	1500	5	750.0	0.3	2.00	0.02
1500	750	5	1500	7	750.0	0.3	5.00	0.03
1500	750	7	1501	8	750.0	0.4	7.00	0.03

3.2.5 Residuals

I define the fit residual in both the time- and frequency-domain to be the difference between the measured and estimated sample pulse,

$$\text{residual} = y_s - T\left(\hat{\theta}\right) y_r \, . \tag{42}$$

Figure 20 shows a typical residual from the fitting algorithm in the time- and frequency-domain. The time-domain residual is expanded vertically by a factor of 20. As expected for a Monte Carlo simulation with only Gaussian white noise, the residuals are approximately flat in the frequency domain and random with no identifiable structure in the time domain. We shall see in the next chapter that the residuals from the experimental apparatus are non-random, suggesting other sources of noise or systematic errors. However, a comparison between the experimental and simulated residuals can guide our analysis, suggesting routes for improvement.

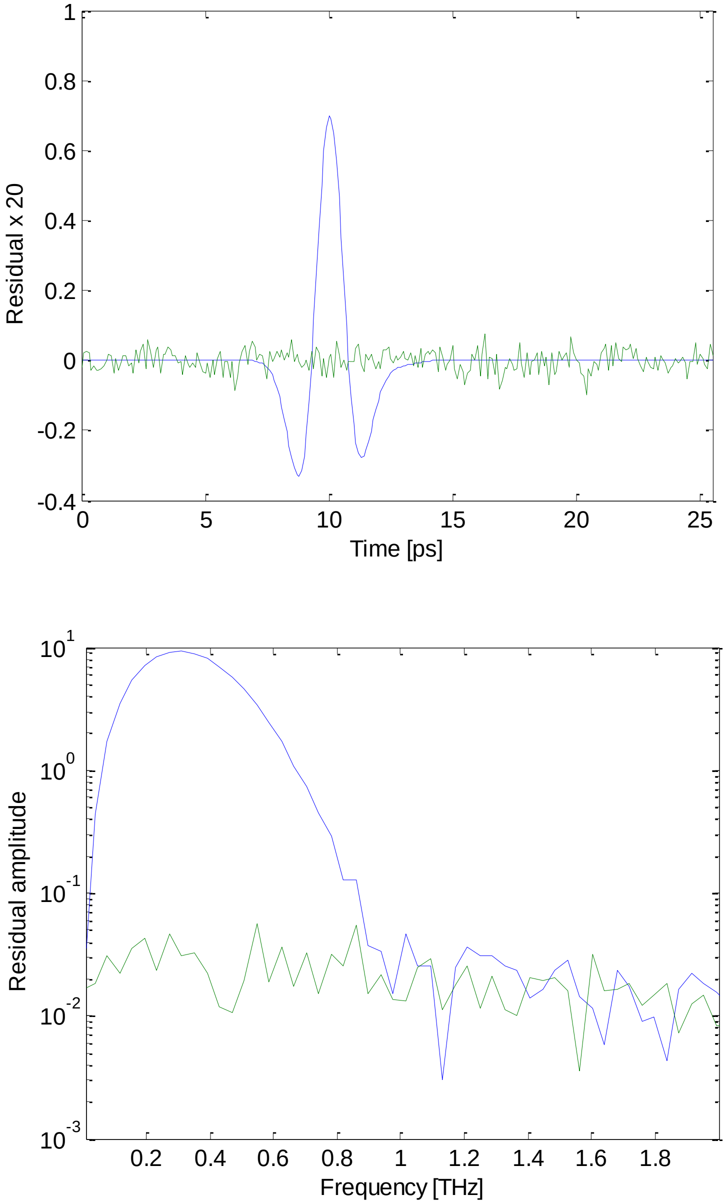

Figure 20 – Time (top, expanded vertically by 20) and frequency (bottom)-domain residuals (green) from Monte Carlo simulation of a 1000 μm sample with 5% moisture content and 750 gsm basis weight, and the respective sample pulse (blue).

3.2.6 Model implications on the fundamental limits of terahertz paper sensing

With the assumptions that this model fully accounts for the physical interactions of the paper and that only Gaussian white noise representing a SNR of 350 is present, the Monte Carlo simulations limit thickness estimates to a precision of 0.3% for thin samples, but almost 1% for thicker samples. Basis weight estimates are within a 0.5 gsm. Moisture content was estimated to better than one-tenth of a percent. A thinner sample contains less total water and therefore the uncertainty in moisture content increases.

From these results, it is clear that the thickness and basis weight estimates should be quite reliable for a large range of samples. In the best case simulated, the standard deviation in the thickness was 2 μm out of 750 μm. Contact caliper gauges are able to achieve submicron resolution for samples up to 1.25 mm thick. The 100 μm sample was estimated with a precision of 0.7 μm. These accuracies are within Honeywell's targets but only the precision on the moisture content for the thicker samples is within the target precision. Further simulations showed the standard deviation in thickness is proportional to the reciprocal of the SNR. An SNR of at least 45000 would be required to achieve a precision of 0.1 μm on the least precise sample simulated.

The simulations described so far assume pulse parameters that are similar to those found in our lab; however, it is possible to generate terahertz pulses with bandwidths of up to 40 THz [21]. I therefore also performed Monte Carlo simulations for different pulse widths w, defined in equation (29). This width of this pulse is inversely proportional to its bandwidth. The pulses were scaled by a factor of $1/w$ to maintain a constant maximum spectral amplitude and therefore a constant SNR. Table 5 shows the results of these simulations, which were performed for a 1000 μm sample with a basis weight of 750 gsm, and 5% moisture content. To accommodate the higher bandwidths, these pulses were generated with 2048 points and a sampling period of 0.05 ps. The fits were performed between 0.1 and 10 THz. Figure 21 shows the bandwidth of pulses with widths of 1 and 0.33 ps. The precision increases with bandwidth, but quickly levels off. The increased precision is less than the improvement expected by simply increasing the SNR. A potential explanation for this effect is that the magnitude of the transmission function, also plotted in Figure 21, is effectively zero above 3 THz, making higher frequencies less relevant. The scattering term, equation (25), varies with ω^2, leading to an absorption that scales linearly with frequency. The transmission function does not decay to zero for Monte Carlo simulations performed without scattering. The wiggles in the transmission function at low frequencies are due to Fabry-Pérot interference.

Table 5 – Results of Monte Carlo simulations for different pulse widths for a 1000 μm thick sample with 750 gsm basis weight, and 5% moisture content. A smaller pulse width corresponds to a larger bandwidth.

Pulse width w [ps]	Precision σ_d [μm]
1.0	2.2
0.33	1.1
0.20	1.1

The transmission amplitude plotted in Figure 21 also suggests that lower frequencies may be more critical to the fit than higher frequencies. The results in Table 4 were found with fits performed between 0.3 and 1.1 THz. Table 6 shows the results of increasing the lower bound on the frequency range for a 1000 μm sample with 5% moisture content and a basis weight of 750 gsm. A small improvement in precision is obtained by expanding the range. The low frequencies are still be excluded, however, since the LLL and Bruggeman models diverge at low frequencies and aberrations, discussed in Appendix B, can add uncertainty to our low frequency data.

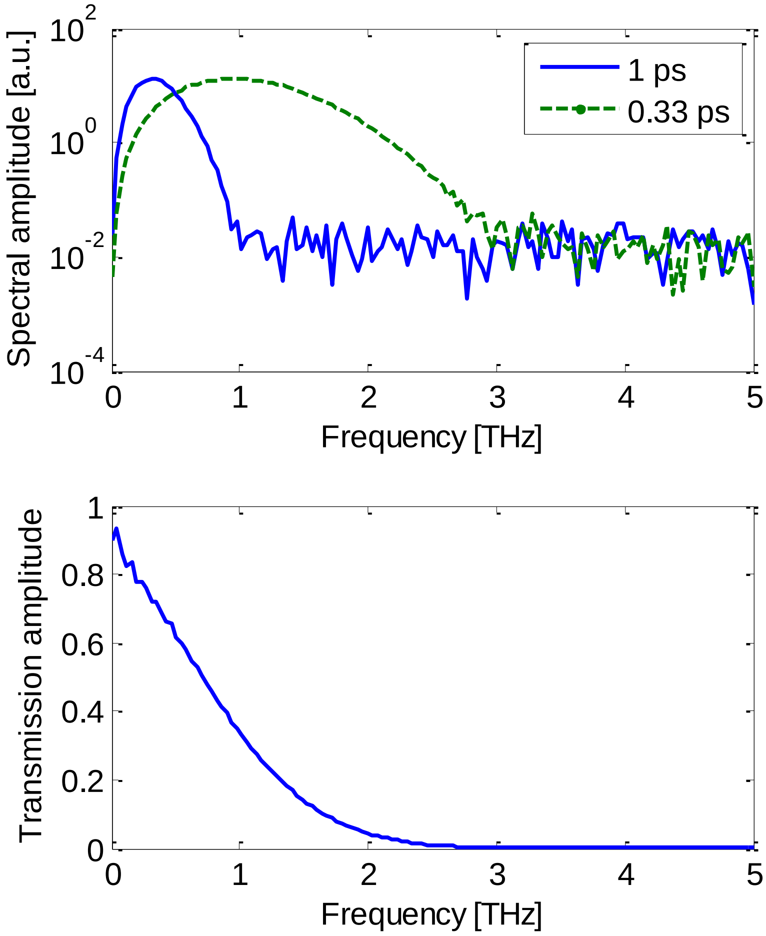

Figure 21 – Spectral amplitude for simulated pulses with different widths (top). Absolute value of the transmission function (bottom).

Table 6 – Precision of Monte Carlo simulations performed over different frequency ranges, from the lower bound to 1.1 THz, for 1000 μm samples with 5% moisture content and a basis weight of 750 gsm.

Lower bound [THz]	σ_d [μm]	σ_M [%]	σ_{BW} [gsm]
0	3	0.02	0.3
0.1	4	0.03	0.3
0.3	4	0.04	0.3

4: TERAHERTZ PAPER MEASUREMENTS

Monte Carlo simulations rely on the assumption that the model accurately reflects the physical interactions of a terahertz pulse with paper. This chapter tests this assumption experimentally. I begin by discussing the samples that I prepared, before using a proof-of-principle measurement to show the plausibility of this model. Next, I detail the algorithm used to estimate the paper process parameters. Finally, I show the results of this algorithm and discuss the current limitations of this model. Currently, large systematic uncertainties appear to prevent more precise parameter estimates.

4.1 Sample preparation

To test whether this model accurately describes real paper samples, I sought samples with the same fibre composition and enough variation in the volume fractions to cover a range of densities. To achieve this, I prepared a set of 12 samples at Honeywell's Centre of Excellence in North Vancouver by compressing samples cut from a single pulp sheet to different thicknesses. The compression was performed on a platen press, which heated both sides of the sample and applied varying pressures for different durations of time. I was able to get a range of thicknesses from 810 µm to 1500 µm, measured independently with a contact caliper sensor at Honeywell.

By fabricating these samples from the same pulp material, I hoped to create a set of samples with a constant moisture content and basis weight but varying thicknesses. These variations would therefore provide a spread in air and fibre volume fractions. Basis weights were measured using a digital scale at Honeywell with samples of known area. The ambient moisture content was determined by measuring the change in mass of the samples after drying in an oven at 106 C overnight. The moisture content is the difference between the ambient and dry mass, divided by the ambient mass. These measurements gave basis weights between 770 and 816 gsm and moisture contents between 6.1% and 6.3%, consistent with the simulated parameters.

4.2 Proof of principle

The goal of this thesis is to show that, in addition to thickness and moisture content, basis weight can also be measured simultaneously using terahertz spectroscopy. This goal rests on the assumption that there will be a measurable difference in paper of different dry content densities.

The change in optical path length, defined in section 3.2.3, between two different samples of thicknesses d_1 and d_2 and indices n_1 and n_2 is

$$\Delta OPL = n_1 d_1 - n_2 d_2 - d_1 + d_2 , \tag{43}$$

which is nonzero for changes that can be measured with terahertz spectroscopy.

From the effective medium theory, equation (23), a change in the volume fraction of any of the components of the mixture will result in a change in the permittivity and thus the refractive index. If a compressed sample is expanded, from thickness d_1 to d_2, the amount of water and fibre remains constant, with air filling the additional space. This reduces the fibre and water volume fractions by a factor of d_1/d_2. The index before and after being expanded, in terms of the initial volume fractions, is therefore

$$\begin{gathered} n_1 = \left(\nu_f \sqrt[3]{\epsilon_f} + \nu_w \sqrt[3]{\epsilon_w} + \nu_a \sqrt[3]{\epsilon_a} \right)^{3/2} \text{ and} \\ n_2 = \left(\frac{d_1}{d_2} \nu_f \sqrt[3]{\epsilon_f} + \frac{d_1}{d_2} \nu_w \sqrt[3]{\epsilon_w} + \left(1 - \frac{d_1}{d_2} \left(\nu_f + \nu_w \right) \right) \sqrt[3]{\epsilon_a} \right)^{3/2} . \end{gathered} \tag{44}$$

Combining this with equation (43) yields the solid line in Figure 22, which shows the change in optical path length for a sample with a basis weight of 789 gsm and 6.2% moisture content. The permittivity was calculated at 300 GHz.

Using the independent thickness measurements for these samples, I measured the refractive index and thus optical path length for each sample using terahertz spectroscopy. Figure 22 also shows the optical path length change calculated using equation (43), with d_1 defined as the thinnest sample. The optical path length change is converted to a timescale by dividing by the speed of light. A path length change of nearly 100 fs occurs for an expansion by a factor of two. The change is well within the temporal sensitivity of our experiment of 2.5 fs, and is qualitatively consistent with the theoretical line.

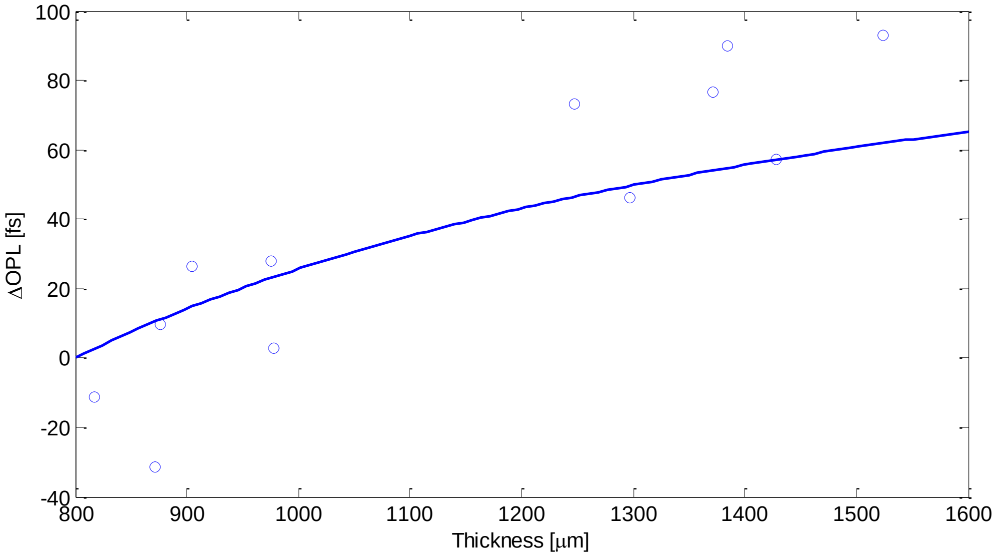

Figure 22 – Optical path length difference (ΔOPL) versus thickness. Solid line gives the theoretical prediction for $d_1 = 800$ μm, BW = 789 gsm, and M=6.2%, and the circles show the measured changes of compressed pulp sheets with respect to the thinnest sheet. Results demonstrate a measurable change, consistent with our expectations that occurs as the density of a sample is varied.

4.3 Fitting algorithm

Our model relies on the knowledge of several physical parameters of a paper sample. In addition to the assumed frequency-dependent permittivities of water and air, the refractive index of the fibre n_f and the scattering parameter τ must be determined independently. These parameters are assumed constant for paper of the same composition and are therefore global fit parameters for a set of samples.

The scattering parameter is determined by iterating the algorithm outlined in this section for τ. The optimal value is determined by minimizing the sum of the squares of the fit residuals, given by equation (42).

To determine the fibre index for these samples, I combined independent process parameter measurements with terahertz data. First, I modelled paper as a two-component wet-dry mixture. This simplified model combines the air and fibre components into a heterogeneous dry mixture. Since d and ν_w are known for each sample, I was able to estimate the refractive index of the dry components for each sample. The global fibre index was then estimated from equation (21), such that

$$\sqrt[3]{\epsilon_{\mathrm{dry}}} = \left(1-\nu_{\mathrm{f}}\right)\sqrt[3]{\epsilon_{\mathrm{a}}} + \nu_{\mathrm{f}}\sqrt[3]{\epsilon_{\mathrm{f}}}\ , \tag{45}$$

where $\nu_a = 1 - \nu_f$. A least squares fit of this equation with the estimated dry permittivities and the known fibre volume fractions provided an estimate for the fibre permittivity, and therefore the fibre index. We assume that the permittivity of the fibre is real, independent of frequency, and the same for each sample [7].

Having determined the fibre index, I obtained estimates of the paper parameters following the procedure outlined in Figure 23. The volume fractions and permittivities for each component are used to generate an effective permittivity based on the LLL model. From the permittivity, we determine the real refractive index, which is used to calculate the scattering absorption. The absorption from the LLL permittivity is then added to the scattering permittivity for a total absorption. The LLL index and combined absorption are then used with a variable thickness to determine the transfer function, which is combined with the frequency-domain sample and reference pulses to calculate the MLE cost function. Taking the standard deviation of the sample and reference pulses in the high-frequency limit (2-5 THz) provides estimates for σ_s and σ_r respectively. This process is repeated to minimize the cost function with respect to d, ϕ, and θ. The angular coordinates are bounded by 0 and $\pi/2$ and the thickness is bounded below by 0. The angle and thickness estimates are finally converted back to process parameters using equation (27). As with any nonlinear minimization procedure, this algorithm is susceptible to local minima, and therefore must be provided with an initial guess of the known parameters.

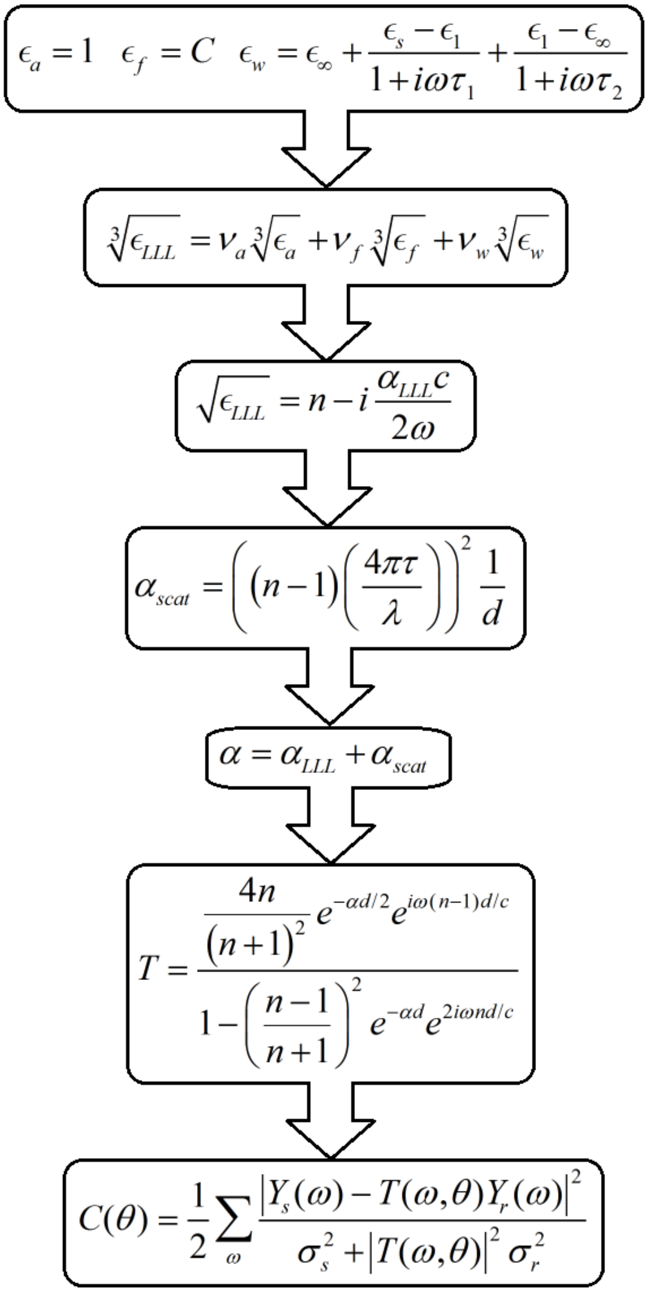

$$\epsilon_a = 1 \quad \epsilon_f = C \quad \epsilon_w = \epsilon_\infty + \frac{\epsilon_s - \epsilon_1}{1 + i\omega\tau_1} + \frac{\epsilon_1 - \epsilon_\infty}{1 + i\omega\tau_2}$$

$$\sqrt[3]{\epsilon_{LLL}} = \nu_a \sqrt[3]{\epsilon_a} + \nu_f \sqrt[3]{\epsilon_f} + \nu_w \sqrt[3]{\epsilon_w}$$

$$\sqrt{\epsilon_{LLL}} = n - i\frac{\alpha_{LLL} c}{2\omega}$$

$$\alpha_{scat} = \left((n-1) \left(\frac{4\pi\tau}{\lambda} \right) \right)^2 \frac{1}{d}$$

$$\alpha = \alpha_{LLL} + \alpha_{scat}$$

$$T = \frac{\dfrac{4n}{(n+1)^2} e^{-\alpha d/2} e^{i\omega(n-1)d/c}}{1 - \left(\dfrac{n-1}{n+1} \right)^2 e^{-\alpha d} e^{2i\omega n d/c}}$$

$$C(\theta) = \frac{1}{2} \sum_{\omega} \frac{\left| Y_s(\omega) - T(\omega,\theta) Y_r(\omega) \right|^2}{\sigma_s^2 + \left| T(\omega,\theta) \right|^2 \sigma_r^2}$$

Figure 23 – Flowchart showing equations used in fitting algorithm . The effective permittivity is calculated from the volume fractions. This yields an index and absorption. This index is used to calculate the scattering absorption, which is added to the absorption from the effective medium theory. The transfer function is then calculated and used with the sample and reference pulses and the noise estimates to minimize the maximum likelihood estimator to obtain estimates for the volume fractions and thickness. Experimental data is used to estimate global values for ϵ_f and τ.

4.4 Terahertz measurements

Figure 24 shows terahertz electric field measurements for the pulp data. The reference pulse and thickest sample (1524 μm) are shown in (a) and the thickest and thinnest (817 μm) samples are shown in (b). The shift in time between the two pulses is caused by the optical path length (OPL) difference between the sample pulses and the reference pulse. Therefore a measurement of the time delay between a sample and reference pulse will relate to the product $n\ d$. From the transfer function given by equation (8), the absorption coefficient causes a change in amplitude. A measurement of the amplitude change therefore relates to the product $\alpha\ d$. Finally, the third free parameter is determined from the frequency-dependence of the transfer function. The two sample measurements shown in Figure 24 (b) are shifted by about 100 fs, consistent with the change in OPL given in Figure 22. Figure 25 shows the Fourier transforms of the three pulses. In both the time and frequency-domains, the thicker sample pulse can be seen to have a larger absorption due to the larger quantity of water present in the sample.

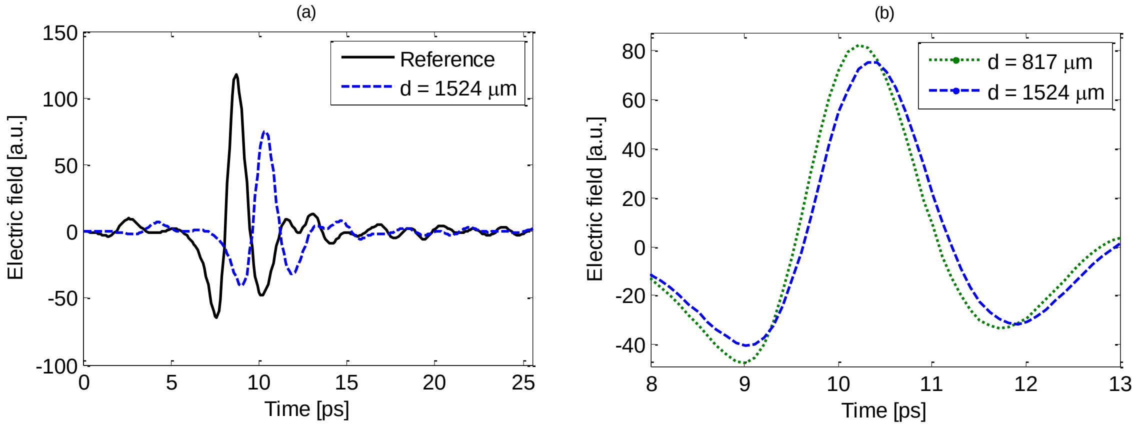

Figure 24 – Measurements of terahertz electric field. (a) shows the reference pulse (black solid line) and 1524 μm thick sample (blue dashes). (b) compares the 1524 μm thick sample with the 817 μm thick sample (green dots).

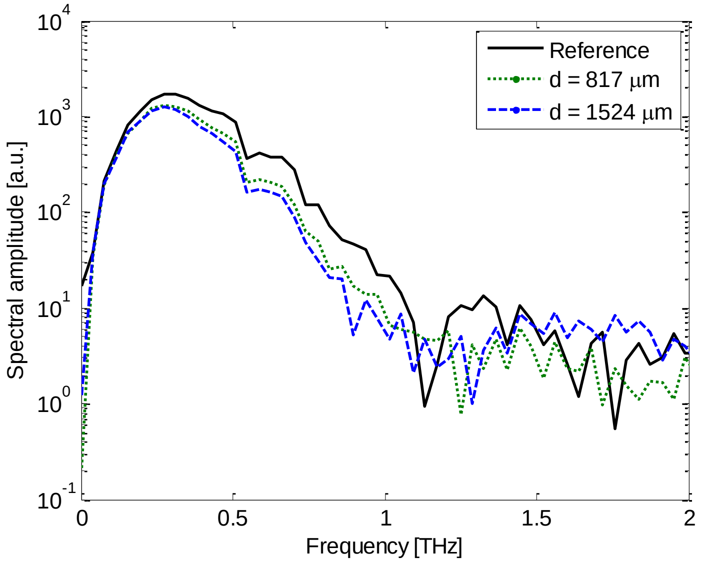

Figure 25 – Frequency-domain measurements of pulp sample data. The solid black line shows the reference pulse, the green dots show the thinnest sample, and the blue dashes show the thickest sample.

4.5 Comparison with the model

Following the prescription in section 4.3, I obtained parameter estimates for each of the paper samples. From two independent terahertz measurements, estimates of the volume fractions and thickness were found for each scan. Finally, the two estimates for each sample were averaged. Only the region of highest SNR, from 300 GHz to 1.1 THz, was included in the fits.

As this is preliminary experimental work with this model, my analysis is less concerned with highly accurate estimates of the process parameters than with finding qualitative agreement between the terahertz estimates and the expected trends from independent measurements. Large discrepancies appear to be due to systematic uncertainties, to which I suggest ways to improve these in the final chapter of this thesis.

Figure 26 shows the volume fraction estimates versus thickness estimates. The solid curves show lines of constant moisture content (6.2%) and basis weight (789 gsm) that correspond to the average of the independent measurements of moisture content and basis weight. We see that the estimates follow the trend of the expected curves, albeit with a slight discrepancy. The fibre volume fraction overestimates the expected value, while the water volume fraction is underestimated.

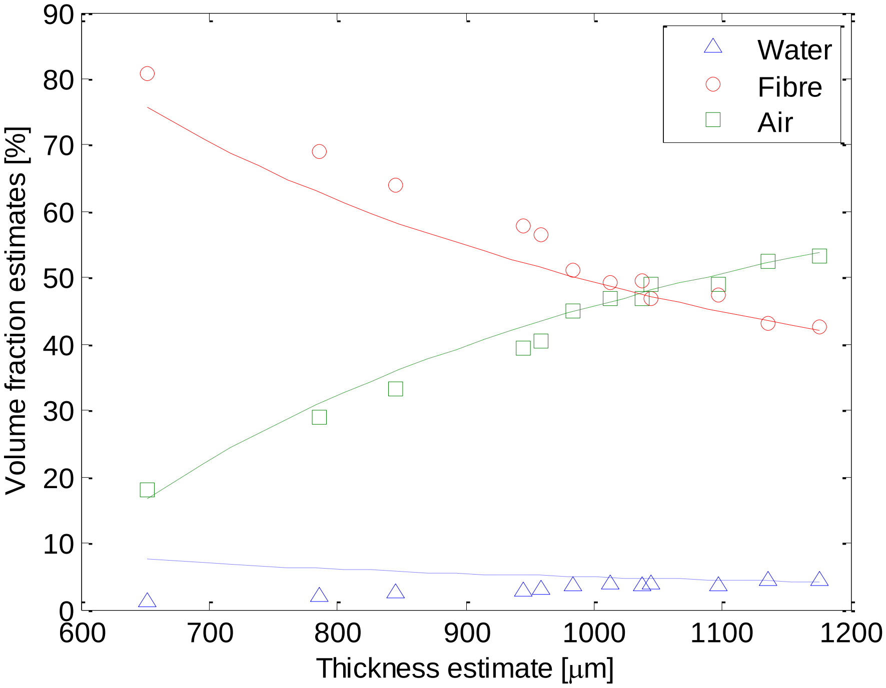

Figure 26 - Volume fraction versus thickness estimates from pulp sample data. Results are shown for water (blue triangles), fibre (red circles), and air (green squares). Solid lines show expected curves for paper with a basis weight of 789 gsm and 6.2% moisture content.

Figure 27 shows scatter plots of both the terahertz estimates and the independent measurements for moisture content, basis weight, and thickness projected on two different planes. From the overestimation of the fibre volume fraction in Figure 26, we should expect the basis weight estimates to be overestimated because fibre is denser than water. This is observed in the bottom plot of Figure 27, which shows the mass scale measurements and terahertz estimates of the basis weights versus thicknesses, which shows that the estimates are generally heavier and thinner than the measured values. Further, because the water volume fraction is underestimated in Figure 26, it is not surprising that the moisture content is underestimated in the top plot of Figure 27. The terahertz estimates also suggest a correlation between thickness and moisture content.

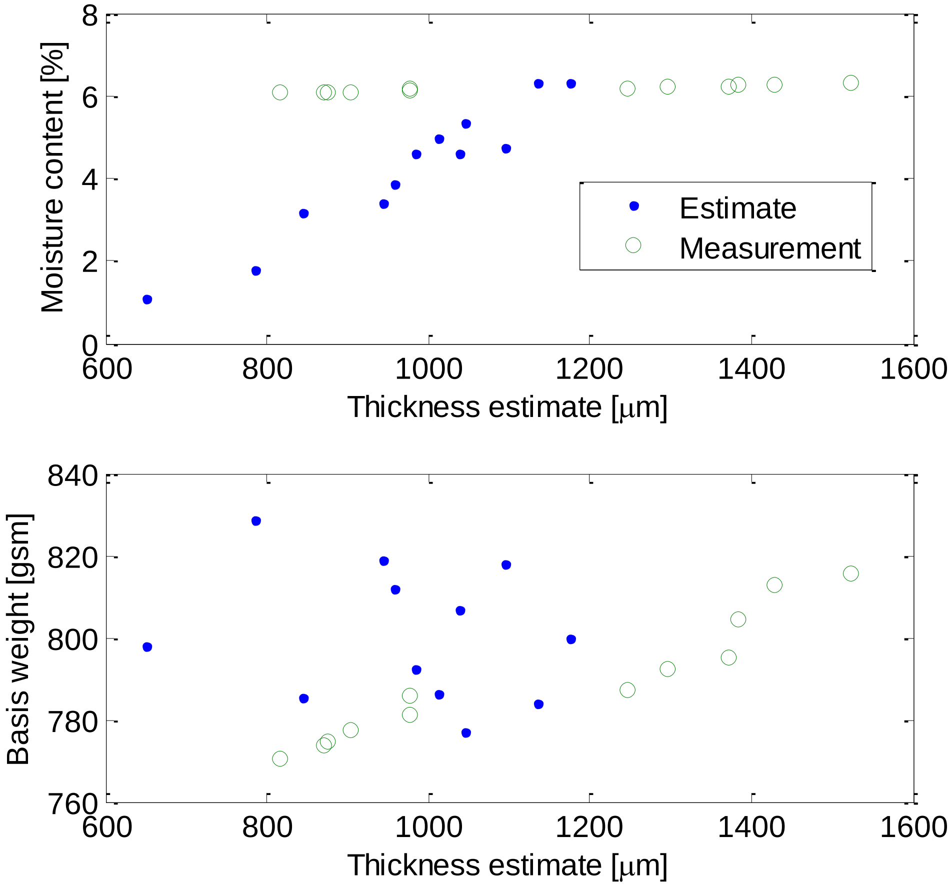

Figure 27 – Paper process parameter estimates for experimental data. Blue dots show terahertz estimates and green circles show independent mass balance measurements of moisture content (top) and basis weight (bottom) versus thickness.

The time- and frequency-domain residuals of these fits, shown in Figure 28, give an indication of the quality of the fits. It is apparent that the fits are not statistically-limited as there are some features in the time-domain residuals near the sample pulse and the low-frequency residuals are above the high-frequency noise floor. The final chapter of this thesis discusses possible causes for this limitation.

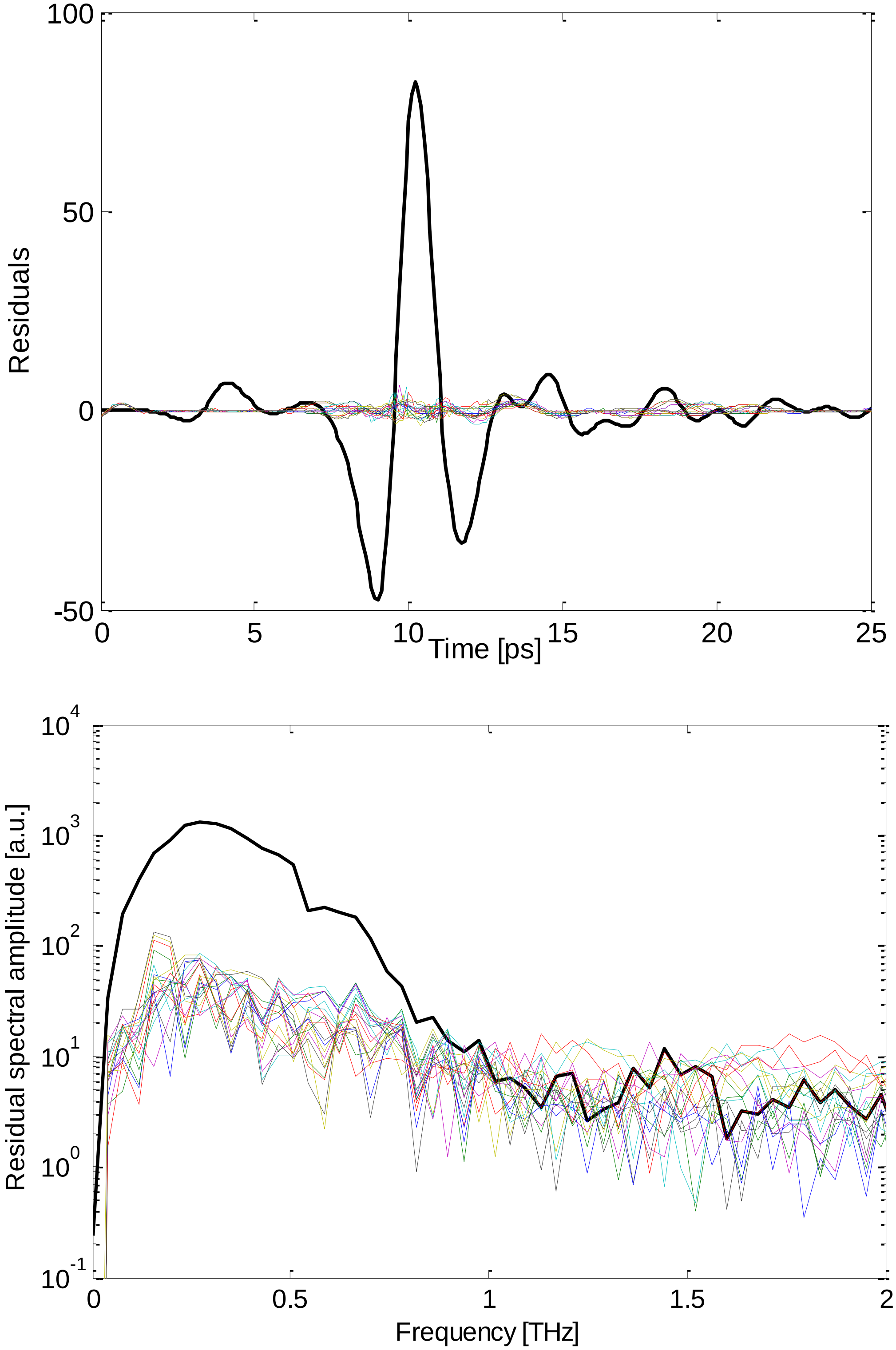

Figure 28 – Time- (top) and frequency- (bottom) domain residuals and averaged sample (bold) pulse and spectral amplitude from pulp samples. Only frequencies between 300 GHz and 1.1 THz were used in the fits.

The improvement afforded by the scattering model can be seen in Figure 29, which shows the time-domain residuals from estimates determined with the scattering parameter set to zero (top, shifted up by +15) and 10 μm (bottom). The additional scattering factor accounts for most of the structure observed in the residuals.

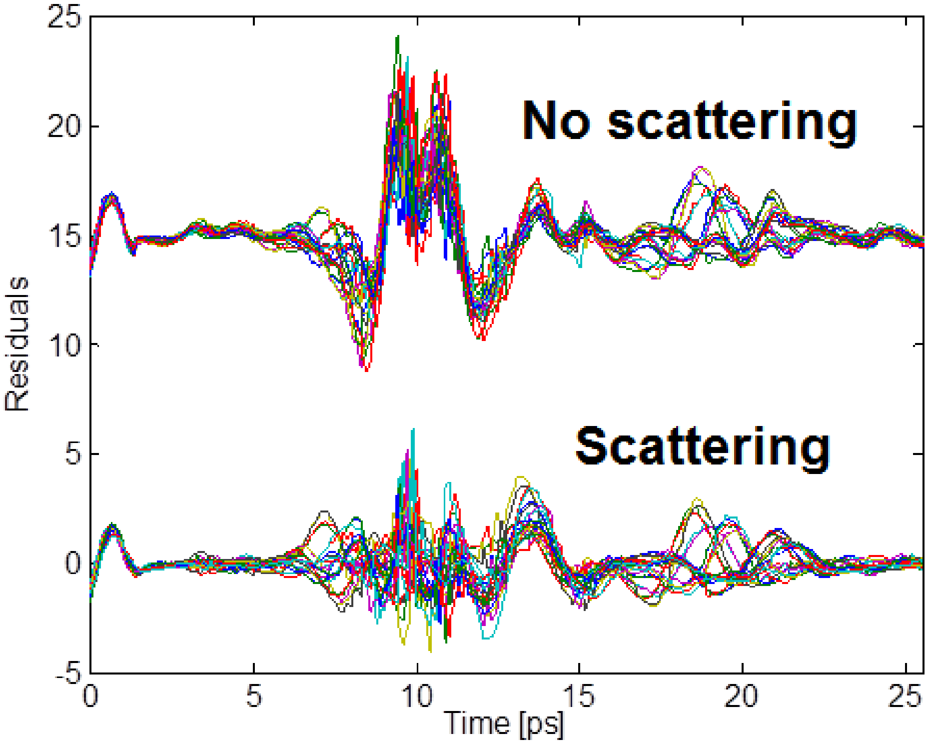

Figure 29 – Comparison of time-domain residuals with and without scattering . The top plot shows the scattering parameter set to 0 (shifted by +15). In the bottom plot τ = 10 μm. The addition of the scattering model accounts for most of the structure of the residuals.

The accuracy of the estimates is estimated by the range of the difference with the independent measurements and as a relative error

$$\text{error} = \frac{\text{estimate} - \text{measurement}}{\text{measurement}} \bullet 100\% . \tag{46}$$

For these samples, the caliper estimates ranged from an underestimate of 590 μm to an overestimate of 170 μm, with an average error of 11%. The basis weight ranged from an underestimate of 29 gsm to an overestimate of 34 gsm, with an average error of 1.5%. Finally, the moisture content ranged from an underestimate of 5% to an overestimate of 0.02%, with an average error of 32%. A larger number of measurements would be needed for better estimates for the precision and accuracy of this algorithm.

5: FUTURE WORK AND CONCLUSIONS

This final chapter will discuss possible avenues of exploration that may improve the accuracy and precision of the results presented in section 4.4. Specifically, the assumptions that went into the models that accounted for scattering and the permittivity of water warrant further development and experimental testing. Additionally, including a more realistic noise model in the Monte Carlo simulations may provide parameter uncertainty estimates that are closer to the observations.

5.1 Scattering model

The additional absorption due to scattering presented in section 3.1.1 potentially presents some complications that have not yet been addressed.

First, as this term modifies only the imaginary portion of the permittivity, it violates the Kramers-Kronig relations, which relate the real and imaginary part of an analytic complex function. A violation of this analyticity implies a causality violation. However, for a scattering parameter of 10 μm, the corresponding imaginary portion of the permittivity due to scattering is four orders of magnitude smaller than the imaginary portion of the permittivity from the effective medium theory, so this violation is negligible.

Secondly, I assumed that the scattering was primarily due to surface effects, but it is plausible that bulk scattering may play an equal or greater role. Equation (25) can be generalized as $\alpha = (\Lambda / \lambda)^2$, with Λ accounting for the physical origin of the scattering. For surface scattering, α is proportional to $1/d$, while for bulk scattering, it should be independent of thickness, since absorption is measured in units of inverse length. Bulk scattering effects should also depend on the density of the fibres. The two effects should be distinguishable by comparing samples of similar surfaces and compositions but different thicknesses.

Finally, this scattering is presented primarily as an additional parameter that can be calibrated to fit the model to the data; however, it is important to verify that we have correctly identified its physical origin. In Jördens et. al., the scattering is proposed to account for effects of surface roughness [14] and τ is a measure of the standard deviation of the thickness. An equally plausible hypothesis is that the scattering arises from the fibres inside the paper. Fibres often align during the manufacturing process, so measurements of the sample at perpendicular orientations may provide an independent verification of the bulk scattering hypothesis if the different paper orientations require different scattering parameter values. Other measurements may even be able to independently determine the size of the fibres.

5.2 Systematic uncertainties

By comparing the residuals of the Monte Carlo simulations, Figure 20, to the residuals from the data estimates, Figure 28, a non-white frequency domain residual can be observed in the data that is not present in the simulation. This suggests that the fit is limited in its precision by a combination of yet unaccounted for sources of uncertainty and systematic errors.

5.2.1 An improved noise model

In the Monte Carlo simulations in section 3.2, the only source of uncertainty added was Gaussian white noise. Realistically, various other sources of noise will contribute to the observed signal. Multiplicative and jitter noise are the most common in terahertz spectrometers; however, flicker (*1/f*) noise may also contribute.

Multiplicative noise scales with the amplitude of the signal. In our lab this noise is primarily attributed to fluctuations in the intensity of the ultrafast pump laser, which causes the amplitude of the terahertz pulse to vary. Vibrations of optical elements on the lab bench induce a temporal shift of several femotseconds in the pulse, referred to as time-base drift. These noise sources can be low-frequency, varying from one scan to the next, over the scale of minutes or less commonly, high-frequency, varying between samples in a single scan.

5.2.2 Perturbations to the model

A close inspection of the time-domain residuals reveals some systematic structure, which potentially cannot be explained with the inclusion of non-white noise. In this case, to achieve greater precision estimates, it may be necessary to revise some of the assumptions that went into the effective medium theory.

First, the water model assumed that the permittivity of water in the paper was that of liquid water. This assumption requires that as water is added to a paper sample, it simply fills the voids of air. In reality water molecules bind to the cellulose until paper reaches a saturation point before it begins to fill the voids. To account for this effect, it may be possible to scale the parameters of the double-Debye model based on empirical findings. To get a better sense of the effect of water on the permittivity of paper, a useful experiment would be to arrange a series of samples of similar composition and thickness but differing water concentrations, and measure the permittivity of each. This could be eased by taking scans of a saturated sample as it dries or a dry sample as it rehydrates with a fast-acquisition spectrometer, capable of doing 1 to 100 scans per second.

Next, the model presented here neglected any absorptive or dispersive effects from the dry components of the paper. Cellulose has a measurable absorption in the terahertz region [22], as well as possible effects from the ash and other components accounted for in the dry component. Other groups have used measurements of compressed, dry samples to account for this absorption, and similar measurements may aid this model [14], [23].

5.3 Conclusion

Using terahertz time-domain spectroscopy and an effective medium theory for paper, I have demonstrated that the caliper, basis weight, and moisture content can be estimated from a single non-contact measurement. Once refined, this technique offers a unique means of determining these parameters in production facilities.

Paper was modelled as a heterogeneous mixture of water, air, and fibrous material, and its electromagnetic response was given by the Landau-Lifshitz-Looyenga effective medium theory with an additional absorptive term due to Rayleigh scattering. Monte Carlo simulations provided statistical limits on the precision of this technique. Experimental data qualitatively agreed with expectations, but exhibited some discrepancies from the simulations. These discrepancies can likely be attributable to additional sources of uncertainty and noise, in addition to simplifications in the models used for the permittivity of water and fibre.

Further investigation should be able to determine the fundamental limits of this technique based on the noise characteristics of a spectrometer, and may provide insight into the accuracy of this model for the terahertz properties of paper.

REFERENCE LIST

[1] Mike Cooke, "Filling the THz gap with new applications," *Semiconductor Today*, vol. 2, no. 1, pp. 39-43, February 2007.

[2] Peter H. Siegel, "Terahertz Technology," *IEEE Transactions on Microwave Theory and Techniques*, vol. 50, no. 3, pp. 910-928, 2002.

[3] Charles Schmuttenmaer, "Exploring Dynamics in the Far-Infrared with Terahertz Spectroscopy," *Chemical Review*, vol. 104, pp. 1759-1779, 2004.

[4] Honeywell Process Solutions. (2007, November) Honeywell Laser Caliper Improves Paper Quality and Production Visibility. [Online]. Accessd on: 25 Nov. 2011. http://hpsweb.honeywell.com/NR/rdonlyres/BE37C273-B087-4DDC-8407-FE3FB4217EE8/55517/SuccessStory_Kanzaki_LaserCaliper.pdf

[5] Honeywell Process Solutions. (2011, August) Moisture Measurement FAQs. [Online]. Accessd on: 25 Nov. 2011. http://hpsweb.honeywell.com/Cultures/en-US/Products/Instrumentation/SensorsPaper/MoistureMeasurement/FAQ/default.htm

[6] Honeywell Process Solutions. (2011, August) Basis Weight Measurement: Frequently Asked Questions. [Online]. Accessd on: 25 Nov. 2011. http://hpsweb.honeywell.com/Cultures/en-US/Products/Instrumentation/SensorsPaper/BasisWeightMeasurement/FAQ/default.htm

[7] P. Mousavi, F. Haran, D. Jez, F. Santosa, and J.S. Dodge, "Simultaneous composition and thickness measurement of paper using terahertz time-domain spectroscopy," *Applied Optics*, vol. 48, pp. 6541-6546, 2009.

[8] Carl-Philippe Kübler, *Creation and characterization of a terahertz time domain spectrometer*. Simon Fraser University: MSc. Thesis, 2003.

[9] F.E. Doany, D. Grischkowsky, and C.-C. Chi, "Carrier lifetime versus ion-implantation dose in silicon on sapphire," *Applied Physics Letters*, vol. 50, pp. 460-462, 1987.

[10] John Frederick Corson, *Advances in Terahertz Spectroscopy of High-Tc Superconductors*. University of California at Berkeley: PhD thesis, 2000.

[11] P. K. Benicewicz, J. P. Roberts, and A. J. Taylor, "Scaling of terahertz radiation from large-aperture biased photoconductors," *Journal of the Optical Society of Amertica B*, vol. 11, no. 12, pp. 2533-2546, 1994.

[12] D. Grichkowsky, Soren Keiding, Martin van Exter, and Ch. Fattinger, "Far-infrared time-domain spectroscopy with terahertz beams of dielectrics and semiconductors," *Journal of the Optical Society of America B*, vol. 7, pp. 2006-2015, 1990.

[13] John H. Scofield, "Frequency-domain description of a lock-in amplifier," *American Journal of Physics*, vol. 62, no. 2, pp. 129-133, 1994.

[14] C. Jördens, M. Scheller, B. Breitenstein, D. Selmar, and M. Koch, "Evaluation of leaf water status by means of permittivity at terahertz frequencies," *Journal of Biological Physics*, vol. 35, pp. 255-264, 2009.

[15] L. D. Landau, E. M. Lifshitz, and L. P. Pitaevskii, *Electrodynamics of Continuous Media*, 2nd ed. Oxford: Pergamon Press, 1984, pp. 42-44.

[16] H. Looyenga, "Dielectric Constants of Heterogeneous Mixtures," *Physica*, vol. 31, pp. 401-406, 1965.

[17] Hans J. LLiebe, George A. Hufford, and Takeshi Manabe, "A model for the complex permittivity of water at frequencies below 1 THz," *International Journal of Infrared and Millimeter Waves*, vol. 12, no. 7, pp. 659-675, 1991.

[18] C. Rønne et al., "Investigation of the temperature dependence of dielectric relaxation in liquid water by THz reflection spectroscopy and molecular dynamics simulation," *Journal of Chemical Physics*, vol. 107, pp. 5319-5331, 1997.

[19] E. Pickwell, B. E. Cole, A. J. Fitzgerald, V. P. Wallace, and M. Pepper, "Simulation of terahertz pulse propagation in biological systems," *Applied Physics Letters*, vol. 84, no. 12, pp. 2190-2192, 2004.

[20] M. A. Gilmore, Saeid Kamal, D. M. Broun, and J. S. Dodge, "Determination of electron-phonon interaction parameters from time-domain terahertz spectroscopy," *Applied Physics Letters*, vol. 88, p. 141910, 2006.

[21] R. Huber, A. Brodschelm, F. Tauser, and A. Leitenstorfer, "Generation and field-resolved detection of femtosecond electromagnetic pulses tunable up to 41 THz," *Applied Physics Letters*, vol. 76, no. 22, pp. 3191-3193, 2000.

[22] B Fischer, M Hoffmann, H Helm, G Modjesch, and P Uhd Jepsen, "Chemical recognition in terahertz time-domain spectroscopy and imaging," *Semiconductor Science and Technology*, vol. 20, pp. S246-S253, 3005.

[23] C. Jördens, S. Wietzke, M. Scheller, and M. Koch, "Investigation of the water absorption in polyamide and wood plastic composite by terahertz time-domain spectroscopy," *Polymer Testing*, vol. 29, pp. 209-215, 2010.

APPENDICES

Appendix A – Mirror mount design

The off-axis parabolic mirrors used to steer terahertz pulses through the spectrometer are made of solid aluminum and are quite massive. The mirrors were originally mounted on simple 1” diameter posts, and counterweights were attached to the back of the mirror to balance the mirror. The mirror assembly acted as a cantilever-oscillator that contributed to the time-based jitter and the mount had more mechanical degrees of freedom than necessary for alignment; therefore, I designed new mounts. The new fixed design, made of solid anodized aluminum, was based on mounts Dr. Frank Hegmann[4] uses at the University of Alberta where I worked as an undergraduate. Based on the technical drawings shown in Figure 30, Laleh Mohtashemi ordered and machined the mounts, with assistance from the SFU Physics machine shop. Figure 31 shows pictures comparing the old and new mount design.

---

[4] Email: hegmann@ualberta.ca

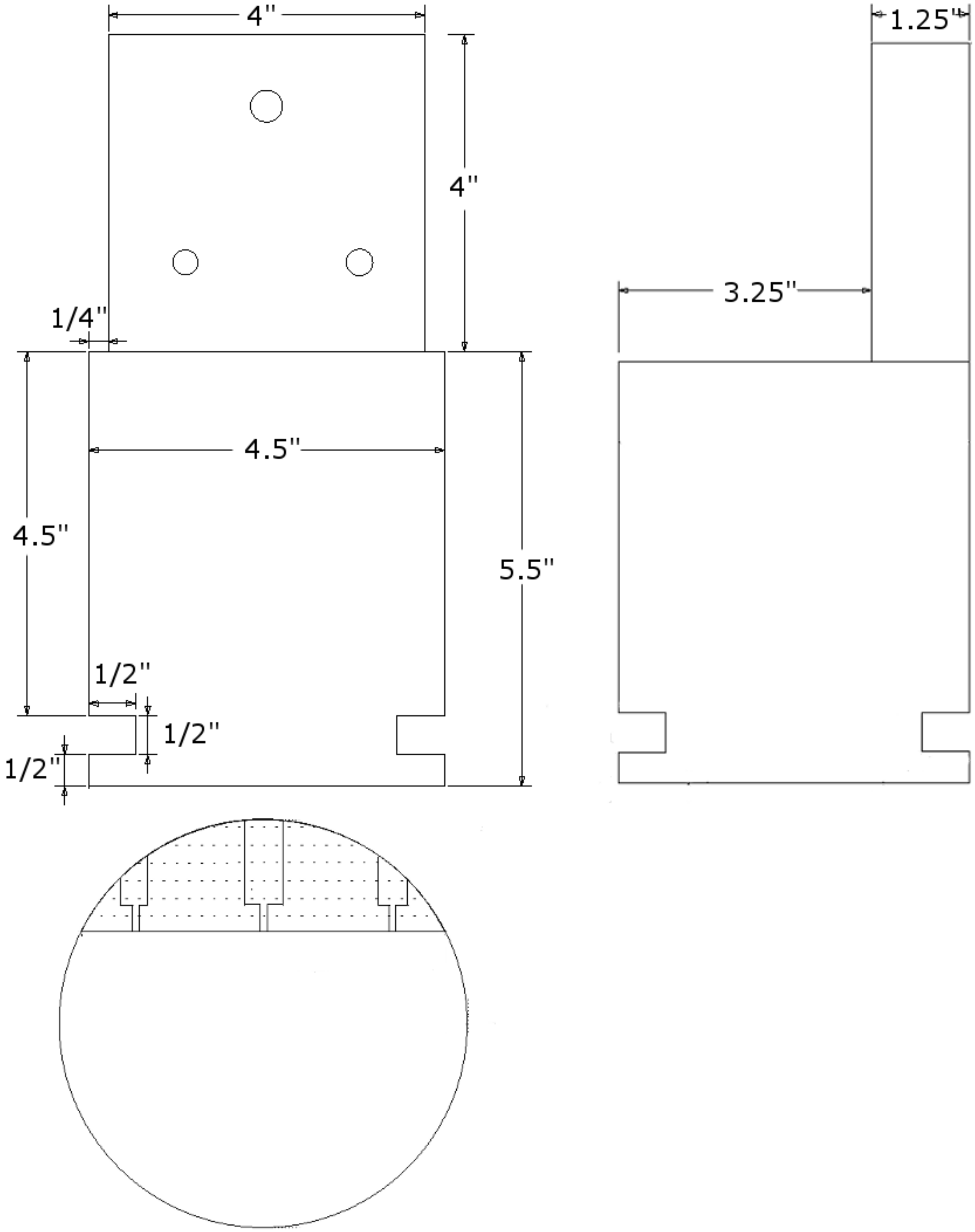

Figure 30 - Schematics for new mirror mount. Screw holes are positioned according to mirror holes and are tapped accordingly.

Figure 31 – Back and front views of old (left) and new (right) mounts (same scale).

The mounts are designed to position the centre of the mirror 6.5” above the optical bench, are 4.5” in diameter, and feature a groove around the bottom that allows the mount to be clamped to the bench. The mounts were anodized for safety to prevent stray laser beams from reflecting from the mount.

Appendix B – Mirror loss calculation

Concerns have persisted that a portion of the terahertz beam may miss the third parabolic mirror in our spectrometer. This prompted me to write a 2-dimensional MATLAB ray-tracing simulation to model these possible losses and to determine their significance. Limiting the simulation to 2 dimensions simplified the analysis, focussing only on the key axis. Figure 32 shows the results of the simulation. Each ray in the simulation takes 1000 steps in 0.05" increments. When a ray is incident on a mirror, the simulation calculates the slope of the mirror and reflects the ray appropriately. Of the 10 initial rays, one can be seen missing the third mirror, suggesting that a portion of the beam may be lost in this configuration.

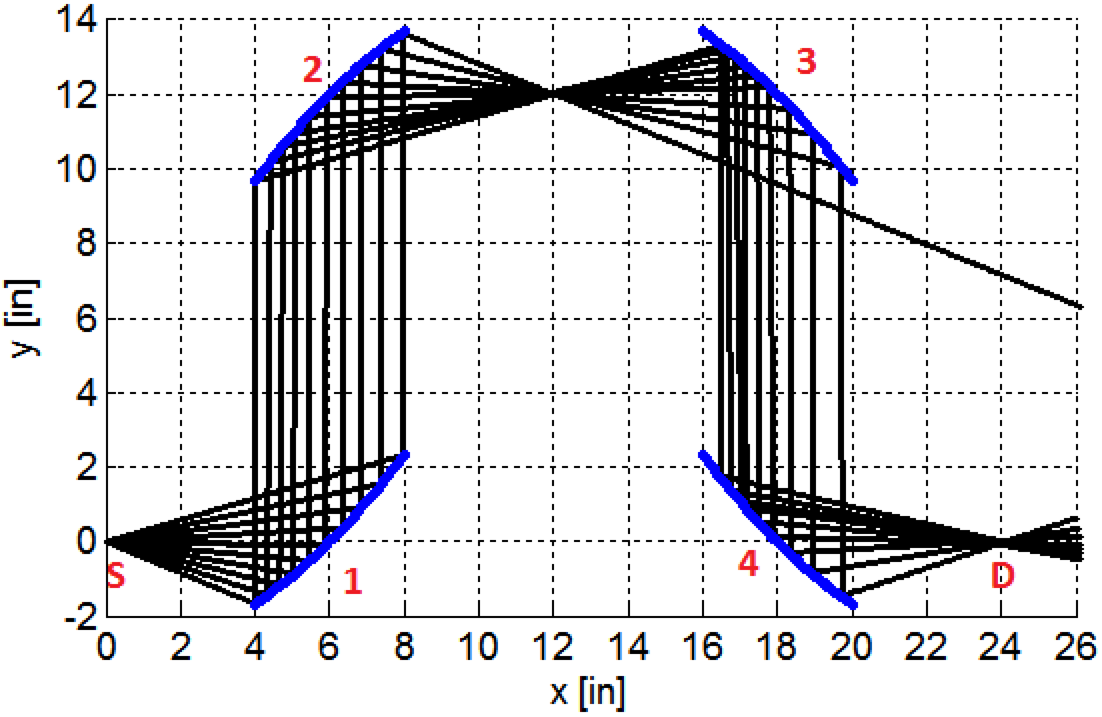

Figure 32 – Results of ray tracing simulation of terahertz spectrometer setup showing lost ray from third off-axis parabolic mirror. Grid units are in inches. Source (S), detector (D), and mirror numbers are marked in red.

To calculate the amount of beam lost from the third mirror, I first need to have an estimate for the size of the beam incident on the second mirror. I therefore took measurements of the terahertz pulse using an iris placed 2" behind the emitter.

Comparing the terahertz amplitude measured at different frequencies for varying iris diameters gives an estimate for the beam size at that location. Figure 33 shows that over 90% of the low-frequency content is detected at 30 mm. The waist is smaller at higher frequencies, so I chose 25.4 mm or 1" as the radius required to account for the majority of the mid-to-high frequency beam. It is worth noting that the waist of the beam is larger at low frequencies, which can introduce aberrations due to the edges of the optic elements. This is part of the reason that low frequency components are excluded in the analysis in sections 3.2 and 4.4.

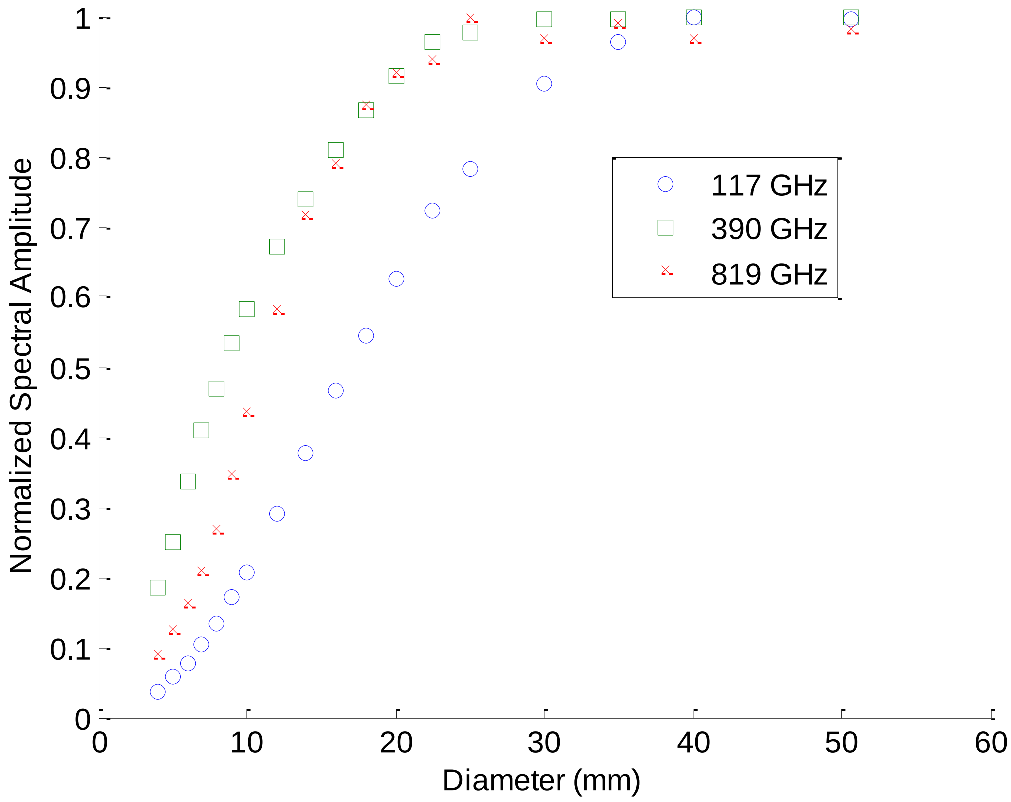

Figure 33 – Beam waist measurements taken 2" from emitter.

Knowing that the mirrors follow a simple parabolic equation (along the axis) of $y = x^2 / (4f)$, where f is the focal length, I calculated the intersection between two rays from the source to the mirror, with an opening angle determined by the waist measurement. Defining the source as the origin, the equations of each ray from the source are given by y_1=4x and y_2=-4x, since the source is 2” from the centre of the 1” iris. Solving the quadratic equations gives intersections at y_1=4.68” and y_2=7.68”, for a collimated beam diameter of 3”.

Figure 34 shows the 3” beam incident on the second mirror. To determine the location of the beam on the third mirror, I again had to determine equations for the two rays: aa’ and bb’. This is simplified by defining the focus as the origin. Using the law of reflection and the slope of the mirror, I determined that aa’ reflects at an angle of 0.2213 radians and bb’ at -0.2838 radians, both with respect to the x-axis in Figure 34. The equations of the two lines are then given by the reciprocal of the tangents of these angles, which, combined with the equation for the parabola (as before), gives intersection points on the x-axis of 4.8” and 8.0”. This just fits within the mirror, whose limits are 4” and 8”.

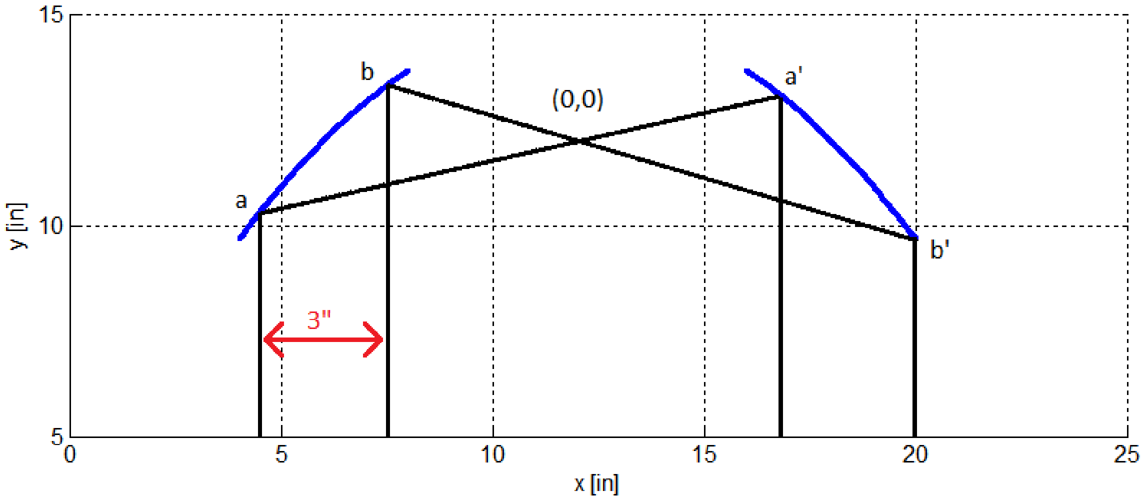

Figure 34 – A 3” collimated beam incident on the second parabolic mirror (top left).

We can therefore conclude that our beam, which almost entirely fits within the 1” iris, will be collected by an aligned third mirror. The minimal losses will be at the lowest frequencies, due to their larger beam size. These results are consistent with Kübler’s analysis [8].